공학박사 학위논문

Source Reconstruction Algorithm Considering Intrinsic Characteristics of Neuroelectromagnetic Source

신경전자기 신호원의 고유특성을 고려한 신호원 복원 알고리즘

2013 년 2 월

서울대학교 대학원

협동과정 계산과학 전공

최 종 호

Abstract

The functional imaging of neuroelectromagnetic sources of electroencephalographic (EEG) and magnetoencephalographic (MEG) based on distributed source models requires additional information and constraints on the source in order to overcome the ill-posedness and to obtain a plausible solution.

In this dissertation, we present two methods to enhance accuracy of MEG and EEG source reconstruction.

We propose a new cortical source imaging algorithm for integrating simultaneously recorded EEG and MEG, which takes into account the different sensitivity characteristics of the two modalities with respect to cortical source orientations. It is well known that MEG cannot reliably detect neuronal sources with radial orientation, whereas EEG is relatively less dependent on the source orientations than MEG. However, this intrinsic difference has not previously been taken into account in the integrative cortical source imaging using simultaneously recorded EEG and MEG data.

On the other hands, most imaging algorithms explicitly favor either spatially more focal or diffuse current source patterns. Naturally, in a situation where both focal and extended sources are present or the source is arbitrary distributed, such reconstruction algorithms may yield inaccurate estimate. The other algorithm proposed in this dissertation improves accuracy of bio-electromagnetic source estimation regardless the extension of source distribution. The additional maximum

amplitude constraint does successively enhance the localization accuracy in EEG/MEG source imaging. The proposed approaches are validated through numerical simulations and applied to practical epilepsy measurements and compared to the resection region. From the extensive analysis, it will be shown that the proposed approaches can enhance the source localization accuracy considerably, compared to the conventional approaches. Therefore the proposed methods in this dissertation are expected to be a promising approach on the research of inverse problem and many clinical applications of EEG and MEG.

Keywords : bioelectromagnetics, source reconstruction method, inverse problem, noninvasive functional brain imaging, EEG, MEG,

Student Number : 2008-30136

Contents

List of Tables

List of Figures

List of Symbols

$\mathbf{E}$	electric field intensity [V/m]
$\mathbf{B}$	magnetic flux density [T]
$\mathbf{J}$	current density [A/m^2]
V	electric potential [V]
$\mathbf{J}^p$, $\mathbf{J}^v$	primary and secondary current density
σ	conductivity in the medium [S/m]
μ	permeability in the medium [H/m]
$\mathbf{x}$	measured electromagnetic signal
$\mathbf{A}$	lead field matrix
$\mathbf{A}^*$	pseudo-inverse solution of $\mathbf{A}$
N_M	number of measurements
λ	hyperparameter (regularization parameter)
$\mathbf{M}$	regularization operator
$\mathbf{W}$	inverse operator
$tr(\cdot)$	trace of a square matrix

1. Introduction

1.1 Motivation and Aim

The functional neuroimaging is a technology to measure an aspect of brain function, often with a view to understanding the relationship between activity in certain brain area and specific brain function. It is primarily used as a research tool in cognitive neuroscience, cognitive psychology, neuropsychology, and social neuroscience and has also been used as powerful tools for studying neural processes in the normal brain as well as clinical applications including treatment of serious neurological and neuropsychological disorders such as epilepsy, depression, and Parkinson's and Alzheimer's diseases.

Brain metabolism and neurochemistry can be studied using radioactively labeled organic molecules, or probes, that are involved in glucose metabolism or dopamine synthesis [1]. Images of dynamic changes in the spatial distribution of these probes transported and chemically modified within the brain can be visualized using positron emission tomography (PET). These images have spatial resolutions as high as 2 mm; however, temporal resolution is highly limited to several minutes. For more direct studies of neural activity, one can investigate local hemodynamic changes. As neurons become active, they induce much localized changes in blood flow and oxygenation levels that can be regarded as the neural activity. Hemodynamic changes can be detected using PET [1], functional magnetic resonance imaging (fMRI) [2], and transcranial optical imaging [3]. Among these, fMRI is currently the most widely

used imaging technique and it can be readily performed using a 1.5T clinical MRI magnet, which can be seen in any general hospitals around us. fMRI studies are capable of producing spatial resolutions as high as 1-3 mm; however, temporal resolution is limited to approximately 1s because of the relatively slow hemodynamic response, when compared to electrical neural activity. In addition to the limited temporal resolution, interpretation of fMRI data is hampered by the complex relationship between the blood oxygenation level dependent (BOLD) changes that are detected by fMRI and the underlying neural activity. Regions of BOLD changes in fMRI images do not necessarily have one-to-one correspondence with regions of electrical neural activity.

Contrary to the techniques described above, the electro-encephalography (EEG) and magnetoencephalography (MEG) measure the electrical neural activity from outside of the head. The MEG measures magnetic field generated by the neural current inside the head using very sensitive magnetic field sensors based on superconductivity [4]. The EEG measures potential differences generated on scalp surface by the neural current and its secondary current flowing through volume conductors (scalp, skull, CSF, and brain) [5]. EEG and MEG have been widely used in clinical and cognitive neuroscience as powerful neuroimaging modalities that can estimate neuronal electrical activities with millisecond temporal resolutions compared to that of PET, fMRI, and NIRS. In particular, EEG and MEG source imaging plays major roles in pre-surgical evaluation and surgical planning for patients with intractable drug-resistant epilepsy, because epileptogenic zones are

only infrequently identified as lesions on structural MR images. In these applications, accurate estimation of neuronal electrical sources is of particular importance to reduce the size of the intracranial EEG grids and to avoid misplacement of the grid electrode locations [6].

Despite their excellent temporal resolution of EEG and MEG, the spatial resolutions provided by EEG and MEG are not comparable to that provided by fMRI, due to limited spatial samplings, uncertainties in the forward modeling and additive noise/artifacts. The spatial resolutions of EEG or MEG can be substantially improved by performing source imaging or by solving an inverse problem to estimate the EEG or MEG sources [7].

Recently developed MEG instruments allow for simultaneous recording of magnetic and electrical fields originating from brain electric activities, and simultaneous EEG and MEG data are routinely recorded in several clinical applications [8]. Several new approaches have been proposed to integrate simultaneously recorded EEG and MEG signals since Wood [9] first used single-channel MEG together with simultaneously recorded EEG to identify underlying neuronal sources in the somatosensory cortex. The use of more physical recordings is expected to enhance the overall localization accuracy compared to single-modality-based localization [10]. However, several studies show that the integrated EEG/MEG imaging method does not always guarantee enhanced localization accuracy [11-16]. Therefore, to successfully integrate EEG and MEG data, a new source imaging algorithm that can accurately estimate neuronal current distributions is required. To

achieve the maximum synergy effect from the multimodal integration of EEG and MEG and thus develop a new imaging algorithm, we considered the different directional sensitivity characteristics of neuroelectromagnetic source.

The methods for solving the EEG/MEG source imaging problems can be categorized in to several models of neuronal source. First, the equivalent current dipole (ECD) model assumes small numbers of current dipoles to approximate the distribution of electrical current in brain. In many studies, it has been successfully applied for estimating neural source activation. The ECD model is very simple to implement and robust to noise. However, the number of ECDs should be determined a priori, which is often difficult due to lack of preliminary information. In addition, final solutions are highly dependent upon initial locations of the ECDs, even when small numbers are localized. Another disadvantage of the ECD model is that it is impossible to estimate the distribution of source in the brain.

In the case of no prior knowledge of the number of source clusters, the current density reconstruction (CDR) approach is known to be appropriate for obtaining reliable solutions. This model assumes numerous current dipoles located in source spaces, usually on tessellated cerebral cortex. Compared to the number of EEG or MEG sensors limited to less than 500, the unknown source activities are usually much more than 5,000 in the CDR model. Therefore, the source estimation problem is known to be underdetermined and ill-posed problem requiring additional constraint on the solution in order to obtain a unique solution. One of the successfully applied constraints which have been used for the CDR models is that

based on the minimum norm of source density. Two famous and popular algorithms, minimum norm estimation (MNE) and minimum current estimation (MCE) choose the source where the L2 and L1 norm of the current distribution is minimized respectively [17, 18]. Various inverse algorithms are proposed to reconstruct the neural source as variations of MNE and MCE, for example, low-resolution electromagnetic tomography (LORETA) [19] and focal underdetermined system solver (FOCUSS) [20]. The reconstructed source with l2 norm minimization, i.e., MNE and LORETA is usually distributed over the whole cortical surface region and blurred. When the source is concentrated to several regions of the brain, L1 norm minimization, i.e., MCE and FOCUSS reconstruct the source more accurately than MNE. Naturally, in a situation when sources are distributed with moderate extension or both focal and extended sources are distributed on the brain, such reconstruction algorithms may yield inaccurate estimate. In this dissertation, we propose a new imaging algorithm to reconstruct the focal or spatially extended sources by adding a constraint of maximum current amplitude to the inverse problem. This algorithm aims at reconstruction the distribution of neural source accurately regardless focal or extended source pattern.

To verify the advantages of two proposed approaches, we applied algorithms to MEG and EEG data simulated with a realistic head model and also applied an algorithm to localize the epileptic activity in a patient with medically intractable epilepsy requiring a respective surgery.

1.2 Overview of Chapters

This dissertation is divided into 5 chapters, references and appendices.

In chapter 2, basic knowledge on physical models for neuroelectromagnetism, which is helpful in order for readers to understand this dissertation is explained. Section 2.1 introduces various techniques that have been developed for imaging brain functionalities. Section 2.2 explains brief history and measuring equipment of EEG and MEG. Section 2.3 describes how neural electrical sources in brain are generated and the several properties of neural source currents.

In chapter 3, conventional mathematical algorithms to solve neuroelectromagnetic forward and inverse problems are introduced. Section 3.1 introduces basic concepts and equations to define the forward problem. Section 3.2 presents conventional inverse methods to reconstruct the source distribution.

Chapter 4 presents the preprocessing steps and quantification metrics to evaluate the reconstructed distributed source. In section 4.1, basic simulation set-ups used in this study and preprocessing step for EEG and MEG analysis are described. In section 4.2, conventional and proposed metrics which is useful to evaluate and quantify the reconstructed sources is presented.

Chapter 5 presents a new cortical source imaging algorithm for integrating simultaneously recorded EEG and MEG, which takes into account the different sensitivity characteristics of the two modalities with respect to cortical source orientations. Numerical simulation results also provided. Numerical case study and massive simulation are presented to evaluate the proposed inverse method.

Chapter 6 presents a new inverse algorithm for the improvement of bio-electromagnetic source estimation regardless the extension of source distribution. The proposed methods is evaluated and compared to the conventional methods through the massive simulation and applied to practical MEG measurements to localize the epileptic zone.

In chapter 7, conclusion of this dissertation is stated based on the results given in chapter 5 and 6.

2. Basics of Functional Neuroimaging

2.1 Functional Neuroimaging

Modern imaging technologies provide the opportunity for non-invasive *in vivo* study and can provide measurements of local neuronal activity of the human brain. These brain imaging modalities can be divided into two global categories.

Structural imaging represents a range of measurement techniques which can display anatomical information of the human brain. These modalities include X-ray, computed tomopraghy (CT), magnetic resonance imaging (MRI) and ultrasound scanning (US).

The other category is functional imaging which investigates human brain function in a noninvasive way. Modalities in this category are based on electrophysiology (EEG/MEG), metabolism (fMRI), and neurochemistry (PET). The imaging techniques have been used as powerful tools for studying neural processes in cognitive neuroscience, cognitive psychology, neuropsychology, and social neuroscience as well as clinical applications including treatment of serious neurological and neuropsychological disorders such as epilepsy, depression, and Parkinson's and Alzheimer's diseases.

Functional imaging represents a range of measurement techniques in which the aim is to extract quantitative information about physiological function. Although high-resolution images are desirable, the emphasis is on the extraction of physiological parameters rather than the visual interpretation of the Structural images.

PET and fMRI measure changes in the composition of blood near a neural event. Because measurable blood changes are slow (on the order of seconds), these methods are much worse at measuring the time-course of neural events, but are generally better at measuring the location. In addition to the limited temporal resolution, interpretation of fMRI data is hampered by the complex relationship between the blood oxygenation level dependent (BOLD) changes that are detected by fMRI and the underlying neural activity. Regions of BOLD changes in fMRI images do not necessarily correspond one-to-one with regions of electrical neural activity [7].

Contrary to fMRI and PET, EEG and MEG measures the electrical brain activity. The EEG measures potential differences generated on scalp surface by the neural current flowing through volume conductors (scalp, skull, CSF, and brain). The MEG measures magnetic field generated by the neural current inside the head using very sensitive magnetic field sensors based on superconductivity (SQUID – Superconducting QUantum Interference Device). They directly measure electrical brain activity and offer superior temporal resolution compared to PET or fMRI. Sampling of electromagnetic brain signals at millisecond intervals is readily achieved and is limited only by the analog-to-digital (AD) conversion rate of the measurements. Resolution is limited by the relatively small number of spatial measurements (a few hundred in MEG or EEG versus tens of thousands or more in PET or fMRI) and the inherent ambiguity of the electromagnetic inverse problem when ECD model is adapted. Table 2.1 summarizes main features of functional neuroimaging modalities

Table 2.1. Comparison of functional neuroimaging modalities

Modalities	Physics	Spatial resolution (mm)	Temporal resolution
PET	neurochemistry	2 ~ 10	20s ~ 1min
fMRI	hemodynamics	1 ~ 3	1s ~ 8s
MEG	neuromagnetics	3 ~ 10	> 1 ms
EEG	neuroelectrics	5 ~ 20	> 1 ms

2.2 Measurement of EEG and MEG

2.2.1 EEG

Electroencephalography (EEG) proposed by hans Berger in 1924 is a non-invasive technique and refers to the recording of the brain's spontaneous electrical activity over a short period of time, usually 20–40 minutes, as recorded from multiple electrodes placed on the scalp [21, 22]. A typical adult human EEG signal is about 10μV to 200 μV in amplitude when measured from the scalp. A commonly used sensitivity of EEG device is 5-10 μV. Since EEG has millisecond-range temporal resolution, EEG has been the most successful clinical tool, especially in studying epilepsy, where seizures are characterized by highly abnormal electrical behavior in neurons in epileptogenic regions. From the initial stages of EEG, the epileptic studies have been main applications of EEG [23, 24].

Many EEG devices are significantly cheaper than all other techniques, therefore, can be used in more places than fMRI, PET or MEG, as these techniques require heavy and immobile equipment. For example, MEG requires equipment consisting of liquid helium-cooled detectors that can be used only in magnetically shielded rooms, altogether costing upwards of several million dollars and fMRI requires the use of a 1-ton magnet in, again, a shielded room. Recenly mobile and wireless EEG recording devices with dry electrodes in Figure 2.1 (a) have been prensented in the field of brain computer interfaces and neurofeedback. [25, 26]

However, the spatial resolution of the EEG techniques is limited due to layers of CSF, skull, and scalp between the electrodes and the current source in the brain.

Consequently, the electrical potential distribution on the scalp is blurred and it is difficult to determine the location of regions of electrically activity. To enhance the spatial resolution, the number of sensor has been increased. As for the sensor configurations illustrated in Figure 2.2 (a), 10-20 electrodes system has been widely used as an international standard, where electrodes are placed at 10 and 20% fractions of the distances between anatomical landmarks of the skull, being nasion, inion, and the pre-auricular points. Recent EEG system provides high density EEG recordings with 256 electrodes as shown Figure 2.2 (b).

Figure 2.1. EEG device with 1 channel (produced by NeuroSky)

Figure 2.2. EEG headcaps: (a) 32 channels (international 10/20 layout) (b) 256 channels (produced by BioSemi)

2.2.2 MEG

EEG scalp voltages are on the order of tens of microvolts and thus readily measured using relatively low-cost scalp electrodes and amplifiers. In contrast, magnetic field generated by neural currents, MEG first measured by David Cohen is very weak, which is ranged from 10fT to 1pT [4]. Note that The Strength of Earth's magnetic field at 0° latitude is about 31μT. To reduce the magnetic background noise, the measurements were made in a magnetically shielded room. At first, a single SQUID detector was used to successively measure the magnetic field at a number of points around the subject's head. This was cumbersome, and in the 1980s, MEG manufacturers began to arrange multiple sensors into arrays to cover a larger area of the head. Recent MEG arrays are set in helmet-shaped dewar that typically contain about 300 sensors, covering most of the head as shown in Figure 2.3. In this way, MEG signals of a subject or patient can now be accumulated rapidly and efficiently.

MEG is much more expensive than EEG, due to expensive equipment with shielded chambers, cryostats, and SQUIDs. On the other hand, MEG measurements are easier to perform without attached electrodes to the skin and spatial resolution is higher than EEG. While EEG is extremely sensitive to the effect of the secondary or volume currents, MEG is more sensitive to the primary current sources in which we are typically more interested.

More recently, MEG and EEG have come to be viewed as complementary rather than competing modalities. Recent MEG systems are equipped for simultaneous acquisition of both MEG and EEG data. As we shall see, inverse methods for the two

modalities are very closely related and can be combined and optimized for hybrid source localization in Chapter 5.

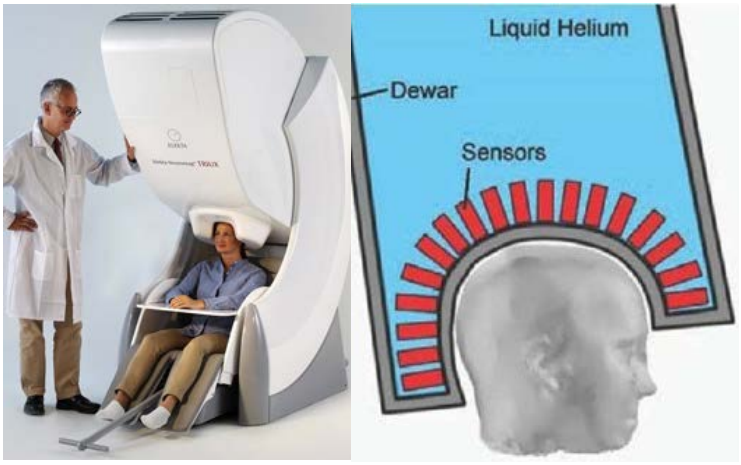

Figure 2.3. Whole-head MEG system produced by Elekta Neuromag (left), and MEG sensors using low-temperature electronics cooled by liquid helium (right). EEG and MEG are recorded simultaneously with 306 MEG channels and 128 EEG channels.

2.3 Anatomy of Human Brain

The human brain consists of about one hundred thousand million nerve cells called neurons. Each neuron consists of a cell body, many short processes of the soma, and a long nerve fiber. The nucleus is embedded in the body or soma of the cell. The cell membrane forms branches called dendrites that project out from the further branches. Furthermore, a single fiber called the axon starts from the stem of the soma. A large number of afferent nerve fibers connect the soma and the dendrites with other neurons or receptor cells via specialized junctions, the synapses. The axon is responsible for transmitting the electrical impulses known as action potentials to other neurons. In the brain, axons typically terminate at synapses on the dendrites, although other types of connections also exist. Figure 2.4 (a) shows a schematic structure of a typical cortical neuron and Figure 2.4 (b) shows arrangement of a neuron. As seen from the figure, the dendrites of cortical neurons generally called pyramidal neurons are parallel to each other, so that they tend to be perpendicular to the cortical surface. Since neurons guide the current flow, the resultant direction of the electrical current flowing in the dendrites is also perpendicular to the cortical sheet of gray matter [28].

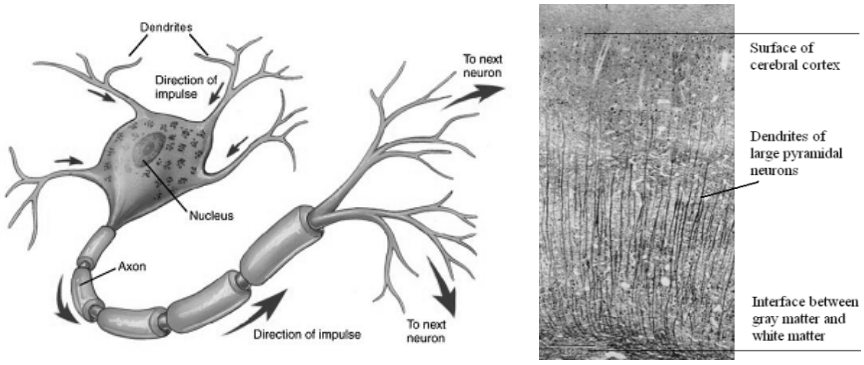

(a) (b)

Figure 2.4. (a) Schematic structure of a typical cortical neuron, and (b) Arrangement of neurons

Most of neurons in human brain (over 90%) are located in the gray matter of cerebral cortex and, as we know, EEG and MEG measures electrical activities generated by the neurons. Thus, to know the structures of cerebral cortex, especially along cortical surface, is very important for neuroelectromagnetic inverse problem. Figure 2.5 shows a human brain viewed from the left side, with main anatomical features identified. In EEG and MEG, we are usually concerned with the uppermost layer of the brain, the cerebral cortex, which is a 2~4 mm thick sheet of gray matter. The cortex has a total surface area of about 2500cm^2, folded in a very complicated way. The folded cortex structure consists of small valleys (sulcus and gyrus) and large grooves called fissures. The longitudinal fissure divides the brain into two hemispheres. The left and right halves are divided into lobes by two deep grooves. The Rolandic fissure runs down the side of both hemispheres, while the Sylvian fissure is almost horizontal. There are four lobes in both halves of the cortex: frontal,

parietal, temporal, and occipital. Most regions of the cortex have been mapped functionally. For example, the occipital lobe is mainly related to visual stimuli (visual cortex). The temporal lobe and parietal lobe are related to auditory stimuli (auditory cortex) and motor-somatosensory stimuli (motor cortex and somatosensory cortex), respectively. The frontal lobe is generally believed to be related to higher brain functions. For more information on the brain anatomy and functions, refer to [28].

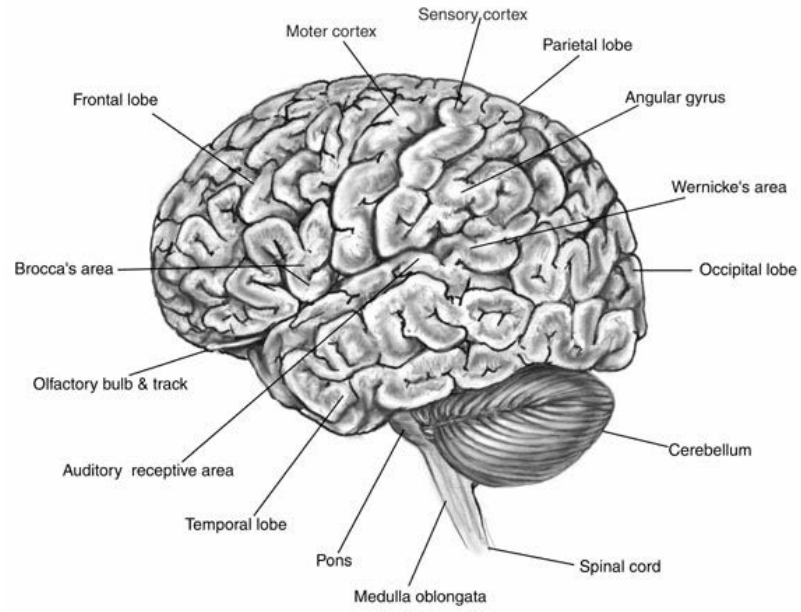

(a)

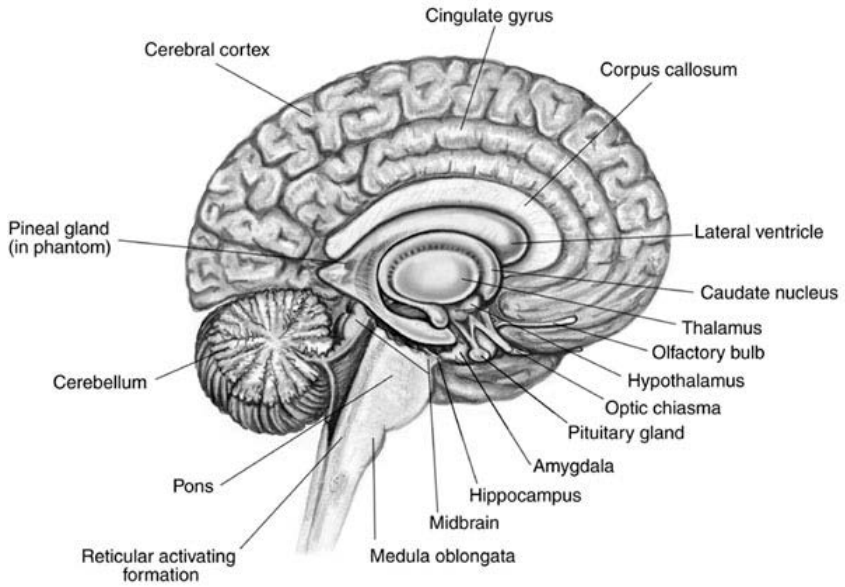

(b)

Figure 2.5. Basic anatomical structures of human brain: (a) View from left side; (b) Cross-sectional view.

From the previous explanations on the mechanisms of neuroelectromagnetic fields, it can be readily imagined that considering volume conduction is very important to calculate electromagnetic field quantities generated by neural currents (usually referred to as forward problems). With respect to different conductivity profiles, the structures of a human head are roughly classified into four different regions: brain, cerebrospinal fluid (CSF), skull, and scalp. Table 2.2 shows typical conductivity values, when assumed that each region has homogeneous and isotropic conductivity [4].

The most important point in the above conductivity profile is that the conductivity of the skull is smaller than the other parts. MEG measures magnetic field generated by the secondary current, and thus the irregular and weak currents in the skull and on the scalp can be ignored as contributors to the magnetic field. Instead, the MEG mainly measures magnetic field produced by primary current.

Table 2.2. Typical conductivity values for different regions

Regions	Absolute Conductivity (S/m)	Relative Conductivity
Brain	0.22	1
CSF	1.79	8
Skull	0.014	1/16
Scalp	0.22	1

2.4 Generation of Neuroelectromagnetic Fields

It is believed that most measurable extracranial fields are generated by the postsynaptic potential, not by the action potential, because the action potentials are not very likely to occur synchronously in large numbers [5, 21]. Also postsynaptic potentials tend to cancel each other in radially symmetric neurons. If, however, large numbers of dendrites are arranged in a parallel way, net effect can be observed. As stated before, dendrites of large pyramidal neurons are arranged perpendicularly to the cortical surface in gray matter. Therefore, if they are activated synchronously, measurable electromagnetic fields can be induced outside the head.

For the cerebral cortex, researchers first focused on clarifying the strength and extension of the actual current source. In a pioneer work, Cooper concluded that a synchronous activation of a cortical area of 6 cm^2 is required to produce observable signal in the human EEG data [29], The threshold cortical area for an interictal spike to be seen by the scalp electrodes is 10 cm^2 [30, 31]. More contemporary studies using simultaneous magnetoencephalographic (MEG) and subdural EEG recordings revealed that just an area of about 4 cm^2 of synchronized cortical activity is necessary to produce an observable MEG signal [32, 33].

Usually, the current-dipole moments required to explain the measured magnetic-field strengths outside the head is 10nAm [4] or 100nAm [34]. Therefore, about a million synapses must be simultaneously active during a typical evoked response. Since there are approximately 10^5 pyramidal cells per mm^2 of cortex and thousands of synapses per neuron, the simultaneous activation of as few as one synapse in a

thousand over an area of one square mil1imeter would suffice to produce a detectable signa1. In practice, activation of larger areas is necessary because there is partial cancellation of the generated electromagnetic fields owing to source currents flowing in opposite directions in neighboring cortical regions. This is also illustrated by a more realistic estimate based on measured current densities, 100-250 nA/mm^2 [4]. Assuming this estimate over the cortical sheet thickness of 1 mm [35], a dipole moment of 10 nAm would correspond to 40 mm^2 of active cortex.

3. Forward and Inverse Problems

In order to estimate neural current sources with measured EEG or MEG signal, mathematical formulation for generation of neuro-electromagnetic fields should be preceeded.

3.1 Neuroelectromagnetic Forward Problem

3.1.1 Quasi-Static Approximation

The useful frequency spectrum for electrophysiological signals in MEG and EEG is typically below 1kHz, and most studies deal with frequencies between 0.1 and 100 Hz. Consequently, the physics of MEG and EEG can be described by the quasi-static approximation of Maxwell equations. The quasi-static approximation can be justified simply by calculating characteristic wavelength of the neuro-electromagnetic fields [4]: When we assume frequency of the neural signals as 100 Hz, the wavelength is 65m, which is much longer than the diameter of the head.

On the other hand, please note that the permeability of the head is that of free space, i.e., $\mu = \mu_0$. By synthesizing these facts, we can rewrite the Maxwell's equations as follows:

$$\nabla \cdot \mathbf{E} = \rho / \varepsilon_0 , \tag{3.1}$$

$$\nabla \times \mathbf{E} = 0 , \tag{3.2}$$

$$\nabla \cdot \mathbf{B} = 0\,, \tag{3.3}$$

$$\nabla \times \mathbf{B} = \mu_0 \mathbf{J}\,, \tag{3.4}$$

where **E** is the electric field intensity, **B** is the magnetic flux density, **J** is the current density, and ρ is the charge density. From (3.2), the electric field can be expressed with a scalar potential,

$$\mathbf{E} = -\nabla V\,. \tag{3.5}$$

The use of V considerably simplifies derivations of formulas for electromagnetic fields.

3.1.2 Analytic Formulation

The forward problem in neuroelectromagnetism is to calculate magnetic field **B**(**r**) or electric potential V(**r**) outside the head from a given primary current distribution $\mathbf{J}^v(\mathbf{r}')$ within the brain. We will assume the whole intracranial volume as piecewise homogeneous conductors. If we assume that the head consists of a set of contiguous regions with constant isotropic conductivity σ_i, i = 1,…,3, representing the brain, skull and scalp for instance, we can derive, from the Biot-Savart law, a relationship between measured magnetic field **B**(**r**) and electric potential on the interfaces of adjacent regions V(**r**′) as:

$$\mathbf{B}(\mathbf{r}) = \mathbf{B}_0(\mathbf{r}) + \frac{\mu_0}{4\pi}\sum_{ij}(\sigma_i - \sigma_j)\int_{S_{ij}} V(\mathbf{r}')\frac{\mathbf{R}}{R^3}\times \mathbf{dS}_{ij}'\,, \tag{3.6}$$

where **r** is the point where the field is computed, R = |**R**| = | **r** – **r**′ |, and the primed

symbols refer to quantities in the source region. The $\mathbf{B}_0(\mathbf{r})$ is the magnetic field due to the primary current only. The second term is the volume current contributions to the magnetic field formed as a sum of surface integrals over the brain-skull, skull-scalp, and scalp-air boundaries. The $\mathbf{B}_0(\mathbf{r})$ can be evaluated as

$$\mathbf{B}_0(\mathbf{r}) = \frac{\mu_0}{4\pi}\int_G \mathbf{J}^p(\mathbf{r}') \times \frac{\mathbf{R}}{R^3} dv' . \tag{3.7}$$

From (3.7), we can see that potentials on interface surfaces should be known to calculate magnetic field at the measuring point $\mathbf{r}$. The interface potentials can be calculated by solving the following integral equation:

$$\begin{aligned}(\sigma_i + \sigma_j)\, V(\mathbf{r}) &= 2\sigma_0 V_0(\mathbf{r}) \\ &\quad + \frac{1}{2\pi}\sum_{ij}{}'(\sigma_i - \sigma_j)\int_{S_{ij}} V(\mathbf{r}')\, d\Omega_{\mathbf{r}}(\mathbf{r}') ,\end{aligned} \tag{3.8}$$

where $\mathbf{r} \in S_{ij}$, and σ_0 is the unit conductivity σ_0 = 1/(Ωm). Note that

$$d\Omega_{\mathbf{r}}(\mathbf{r}') = -|\mathbf{r} - \mathbf{r}'|^{-3}\,(\mathbf{r} - \mathbf{r}') \cdot \mathbf{dS}'_{ij} \tag{3.9}$$

is the solid angle subtended at $\mathbf{r}$ by the surface element $\mathbf{dS}'_{ij}$ at $\mathbf{r}'$.

$V_0(\mathbf{r})$ is a primary potential due to the primary current in an infinite homogeneous medium with unit conductivity and can be expressed as

$$V_0(\mathbf{r}) = \frac{1}{4\pi\sigma_0}\int_G \frac{\nabla' \cdot \mathbf{J}^p(\mathbf{r}')}{R} dv' . \tag{3.10}$$

The simplest approach to calculate magnetic fields or electric potentials outside the head is to assume the head as a single sphere or a set of nested concentric homogeneous spherical shells. Then, the basic equations given in (3.6) and (3.8) can be solved by simple analytic formulas. This rough assumption is sometimes useful for many clinical and research applications, especially when heavy iterative processes are required.

In the homogeneous single sphere, the magnetic field induced by a current dipole **Q** can be expressed as

$$B(r) = \frac{\mu_0}{4\pi} \frac{F\mathbf{Q} \times \mathbf{r}_Q - (\mathbf{Q} \times \mathbf{r}_Q \cdot \mathbf{r}) \nabla F(\mathbf{r}, \mathbf{r}_Q)}{F(\mathbf{r}, \mathbf{r}_Q)^2}, \tag{3.11}$$

where

$$F(\mathbf{r}, \mathbf{r}_Q) = a(ra + r^2 - \mathbf{r}_Q \cdot \mathbf{r}), \tag{3.12}$$

with $\mathbf{a} = (\mathbf{r} - \mathbf{r}_Q)$, $a = |\mathbf{a}|$, and $r = |\mathbf{r}|$ [36]. An interesting point in (3.11) is that radial primary current does not generate any magnetic field. This is true for any axially symmetric current in an axially symmetric conductor. Recent studies have insisted that the spherical volume conductor model could substitute for a realistic head model, especially in MEG study [37].

Likewise, the surface electric potential generated by the current dipole Q can be expressed as

$$V = \frac{\mathbf{Q}}{4\pi\sigma} \bullet \{ 2\frac{\mathbf{a}}{a^3} + \frac{1}{r^2 a}[\,\mathbf{r} + \frac{\mathbf{r}\, r_Q \cos\varphi - r\,\mathbf{r}_Q}{r + a - r_Q \cos\varphi}\,]\}, \qquad (3.13)$$

where φ is the angle between $\mathbf{r}$ and $\mathbf{r}_Q$ [38]. Contrary to MEG cases, to use the spherical conductor model in EEG, positions of electrodes should be modified. However, such modification may yield rather severe errors because general shapes of the heads are close to ellipsoids, not spheres. Moreover, the results of forward calculation in EEG are highly influenced by the relatively low conductivity of the skull, and thus the rough approximation has proved to be inadequate for EEG studies.

3.1.3 Numerical Approach

The boundary element method (BEM) offers the opportunity to account for the individual, non-spherical shape of the main inter-tissue boundaries within the head, such as scalp surface, inner and outer boundaries of the skull, surface of the brain, and possibly ventricles. Each of the boundaries is discretized into triangular elements. Figure 3.1 shows an example of a typical 3-layer model [39].

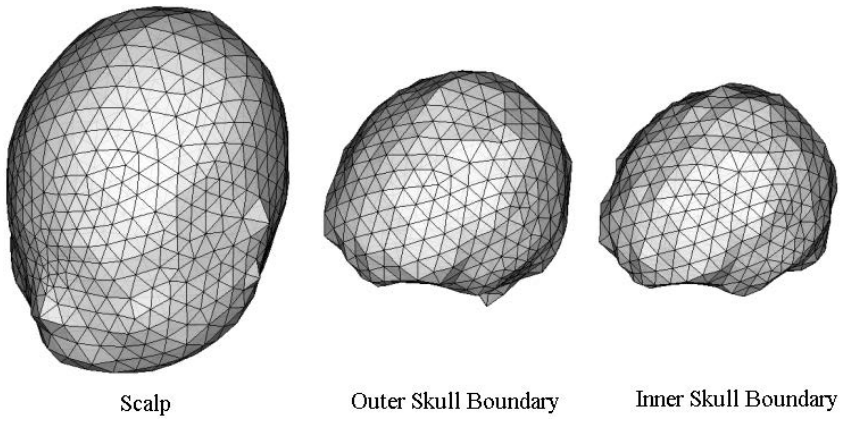

Figure 3.1. A typical boundary element model of human head. Brain surface is generally excluded in the BEM model.

To calculate magnetic fields induced by neural source in MEG, equation (3.6) should be solved. To calculate (3.8), surface potentials should be evaluated at all elements using (3.8). The process is very straightforward and thus the magnetic fields can be easily evaluated using simple surface integrations. In EEG, the surface potentials calculated from (3.8) can be directly used to evaluate the scalp potentials. In any cases, the equation (3.8) should be solved using the BEM.

For a node *k*, the (3.8) can be discretized as

$$(\sigma_{i,k}+\sigma_{j,k})V_k = 2\sigma_0 V_{0,k} + \frac{1}{2\pi}\sum_{ie=1}^{N_e}(\sigma_i^{(ie)}-\sigma_j^{(ie)})\int_{\Delta_{ie}} V(\mathbf{r}')d\mathbf{S}'_{ie}\,, \quad (3.14)$$

where N_e is the number of elements, *ie* is the element index, and the integration term represents a surface integral over the element.

Although the finite element method (FEM) is the most widely used approach to

solve various kinds of differential equations in many engineering research fields, it has rarely been applied to the analysis of neuroelectromagnetic fields [40, 41]. The main reason is that generating tetrahedral elements is much more difficult than generating triangular elements for the BEM. Moreover, to detail complex structures inside the human head, great number of elements and nodes are required, yielding higher memory requirement and heavy computational burden. The main advantage of the FEM is that it can consider the inhomogeneity and anisotropy of the brain tissue, especially anisotropy of white matter originated from neuronal fibers. To estimate the fiber track, recently developed technique based on diffusion tensor MRI (DT-MRI) technology has been studied. The DT-MRI probes the microscopic diffusion properties of water molecules within the tissues of the brain. The conductivity of the tissues can then be estimated by the diffusion values [42]. However, this technique is still under investigation and at the present level of analysis, we largely ignore these complications.

Some researchers have tried to apply the finite volume method (FVM) for the MEG/EEG forward problems [43, 44]. The FVM can also consider anisotropic volume conduction. Contrary to the FEM, the FVM can always ensure continuity of secondary current flow, which is physiologically more plausible. However, it has a critical problem that kinds of possible elements are highly restricted – either prism elements or brick elements.

When all the above facts are considered, the BEM is thought to be currently the most adequate method to solve the MEG/EEG forward problems. Hence, all the

forward calculations that will be presented in this dissertation are based on the BEM.

3.1.4 Linearization of Forward Problem

Regardless of the head model, the electric potential and the magnetic field measurements are often assumed to be linear with respect to the dipoles moment **j**. The electric potential or magnetic field observed at **r** can be expressed as:

$$s(\mathbf{r}) = \mathbf{a}(\mathbf{r}, \mathbf{r}')^T \mathbf{j}, \tag{3.15}$$

where **a**(**r**,**r**') is a gain vector obtained as the solution to either the electric or magnetic forward problem for a dipole located at **r**'. For multiple dipoles located at $\mathbf{r}_i$, the observation is simply linear of the individual contributions given by

$$s(\mathbf{r}) = \sum_i a(\mathbf{r}, \mathbf{r}_i')\, j_i . \tag{3.16}$$

For The EEG or MEG measurements at n_s sensor, the observation generated by n_x dipoles can be expressed with matrix multiplication as follows:

$$\mathbf{s} = \begin{bmatrix} s(\mathbf{r}_1) \\ \vdots \\ s(\mathbf{r}_{n_s}) \end{bmatrix} = \begin{bmatrix} \mathbf{a}(\mathbf{r}_1, \mathbf{r}_1) & \cdots & \mathbf{a}(\mathbf{r}_1, \mathbf{r}_{n_x}) \\ \vdots & \ddots & \vdots \\ \mathbf{a}(\mathbf{r}_{n_s}, \mathbf{r}_1) & \cdots & \mathbf{a}(\mathbf{r}_{n_s}, \mathbf{r}_{n_x}) \end{bmatrix} \begin{bmatrix} j_1 \\ \vdots \\ j_{n_x} \end{bmatrix} = A\mathbf{x}. \tag{3.17}$$

In this dissertation, EEG and MEG leadfield matrix, *A* is calculated using (3.6) and (3.8).

3.2 Neuroelectromagnetic Inverse Problem

Finding underlying neural sources from given EEG/MEG data is called EEG/MEG inverse problems which are known to be ill-posed problems. The ill-posed problems can generally be solved by introducing priors on the solutions. This chapter describes several approaches in EEG/MEG inverse problem with CDR model. source imaging with CDR model assume that unknown sources are distributed in space and the unknwon parameters are the strengths of the distributed sources.

3.2.1 Distributed Source Model

Distributed source model, sometimes referred to as current density reconstruction, assumes a lot of scattered (or distributed) dipole sources with fixed locations and/or orientations in the whole brain volume or on the cortical surface, and then estimates their amplitudes from the data. This approach does not require any *a priori* information on the numbers and locations of dipoles.

Dale and Sereno [45] first proposed constraining the source space into anatomically known locations (interface between white and gray matter of cerebral cortex) and orientations (perpendicular to the cortical surface). The anatomically constrained distributed source model is usually called a cortically distributed source model. Therefore the distributed source reconstruction problem can be stated as

$$\mathbf{s} = A\mathbf{x}, \tag{3.18}$$

where $\mathbf{s}$ is n_s by 1 measurement vector containing the electric potentials or magnetic field, $\mathbf{x}$ is a n_x by 1 solution vector representing magnitude of normally oriented

neuronal current density distributed on the cortical surface, A is the leadfield matrix representing the system transfer coefficients from each source to each measuring point.

Although the measured data **s** do not give the source strengths **x** unambiguously if the number of discretized sources is larger than the number of sensors, a minimum norm estimate of **x** can be calculated as a solution of

$$\min \ \|\mathbf{x}\| \quad \text{subject to} \quad \mathbf{s} = A\mathbf{x}. \tag{3.19}$$

This approach has different forms depending on which norm is selected.

3.2.2 L2 Norm Minimization Approach

The concept of the distributed source model was originated by Hämäläinen and Ilmoniemi's study [46]. They assumed a lot of dipole sources distributed at regular points, or volume pixel (voxel), and estimated the orientations and magnitudes of their moment vectors using minimum norm estimation (MNE), which selects the solution where the L2 norm of the current distribution was smallest. When the L2 norm is adapted, the minimum L2 norm solution solves optimization problem

$$\min \ \|\mathbf{x}\|_2 \quad \text{subject to} \quad \mathbf{s} = A\mathbf{x}. \tag{3.20}$$

A well-known procedure for determining the minimum or maximum of a function subject to equality constraints is the Lagrange multiplier method.

We introduce Lagrange multipliers:

$$L(\mathbf{x}, \lambda) = \mathbf{x}^T\mathbf{x} + \lambda^T(A\mathbf{x} - \mathbf{s}) \tag{3.21}$$

and optimality conditions are

$$\frac{\partial L}{\partial \mathbf{x}} = 2\mathbf{x} + A^T \lambda = 0\,, \tag{3.22}$$

$$\frac{\partial L}{\partial \lambda} = A\mathbf{x} - \mathbf{s} = 0\,. \tag{3.23}$$

From (3.22),

$$\mathbf{x} = -\frac{A^T \lambda}{2}\,, \tag{3.24}$$

by substitute into (3.23) to get

$$\lambda = -2(AA^T)^{-1}\mathbf{s}\,, \tag{3.25}$$

Hence the L2 norm minimum solution is

$$\mathbf{x} = A^T (AA^T)^{-1}\mathbf{s}\,. \tag{3.26}$$

Under the situation that sensor data is corrupted by noises can be found in Appendix A.

3.2.3 L1 Norm Minimization Approach

The minimum current estimate minimizes the sum of the absolute currents (L1 norm) [18, 47]. This leads to more focal source estimates than estimates using Euclidean (L2) norm and can represent well the relatively compact source areas typically activated. L1 and L2 solutions are presented and compared in Chapter 6.

When the L1 norm is adapted, the minimum L1 norm solution solves optimization problem

$$\min \ \|\mathbf{x}\|_1 \quad \text{subject to} \quad \mathbf{s} = A\mathbf{x}. \tag{3.27}$$

But iterative methods would be needed to calculate L1 norm minimization problem. Well-known procedures for determining this L1 minimum solution subject to equality constraints are simplex method and interior point method [48, 49]. The conversion of (3.27) to general linear programming (LP) problem under the noise corrupted situation can be found in Appendix C.

4. Preprocessing and Quantitative Evalution Metrics

4.1 Preprosessing

Neuroelectromagnetic inverse problems are hard to verify using *in vivo* experiments because exact source locations inside a human brain are not known *a priori*. Therefore, artificially-constructed forward data have been widely used to validate MEG and EEG inverse algorithms. Hence, we applied the new inverse method introduced in the previous section to artificially constructed EEG and MEG data sets. The MEG sensor layout used for the simulation was adopted from a commercial 148-channel whole-head magnetometer system (Magnets 2500 WH; Biomagnetic Technologies, San Diego, CA). EEG sensors were generated by projecting the 148 MEG sensors to the nearest points on the scalp surface to allow for a direct comparison of the performances of the two modalities.

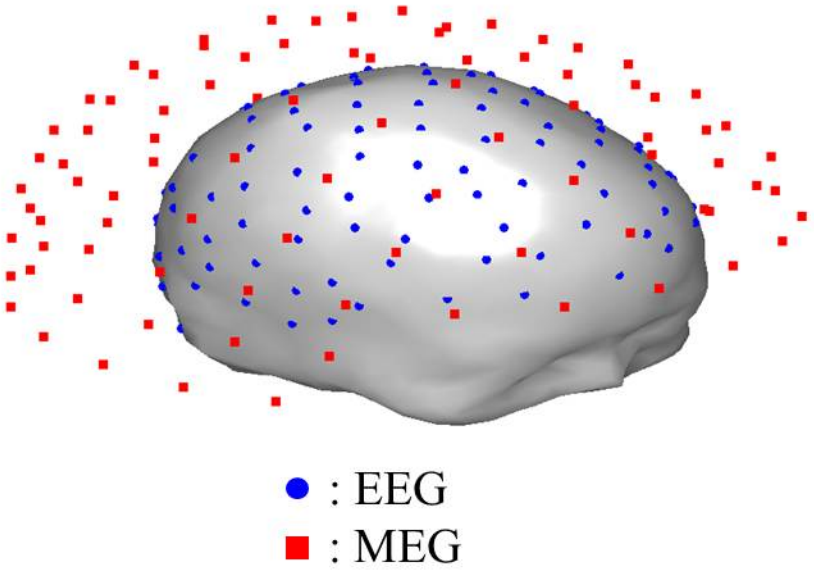

Figure 4.1. Layout of 148 channel EEG and MEG sensors

We extracted the interface between the white and gray matter from structural MRI images of a standard brain atlas (180*217*180 pixels, 1*1*1 mm) provided by the Montreal Neurological Institute (MNI). To extract and tessellate the cortical surface, we used CURRY6 for Windows® (Compumedics, Inc., El Paso, TX). Although advances in medical image processing and high resolution structural MRI allow high resolution cortical surfaces with sub-millimeter modeling errors to be obtained, it is computationally inefficient to use whole cortical surface vertices for source reconstruction purposes because of the underdetermined relationship between a limited number of sensors and a larger number of source locations. To reduce the number of possible source locations, a smaller number of vertices was downsampled from the cortical surface as regularly as possible and used only for source

reconstruction purposes, whereas the original mesh information was used only for visualization purposes. In the simulation study, we sampled 11,373 vertices and 22,774 triangular elements from the original dense cortical vertices. For the accurate forward calculation, we applied a first-order node-based boundary element method (BEM) to calculate the forward magnetic field and electric potential distributions [50]. We obtained EEG and MEG leadfield matrices by applying BEM to three-layer tessellated boundary surfaces, consisting of the inner and outer skull boundaries and scalp surface, which were generated from the same MRI data using CURRY6. A total of 3,393 nodes were used for the node-based BEM computation. The relative conductivity values of the brain, skull, and scalp were assumed to be 1, 1/16 and 1 (S/m), respectively, as mentioned in Table 2.2.

We assumed that current sources were constant cortical patches composed of a set of dipoles with constant dipole moments and orientations perpendicular to the cortical surface. To generate activation patches and construct a forward data set, we adopted the concept of a virtual area. The activation patch was generated using the following process: 1) a point was selected as a seed of an activation patch; 2) the patch was then extended to include neighboring vertices around the patch; 3) if the total virtual area of the cortical patch exceeded the targeted surface area, the extension of the activation patch was terminated [51]. Because some cortical surface regions were too distant from sensors to generate detectable EEG and MEG signals in a noisy environment, a limited numbers of source patches were chosen, from which the distance to the scalp surface did not exceed 30 mm. Source patches on the

cerebellum were also excluded.

The numerical simulation is performed using MATLAB 2012a on Microsoft Windows 7 with Intel Core 2 Duo 3.16G MHz CPU clock rate and 8G RAM.

4.2 Techniques of Quantification of Distributed Source

When a new source imaging algorithm is proposed, the performance of the inverse algorithm need to be verified and compared with those of the existing ones. For the evaluation of the reconstructed sources, evaluation metrics or error metrics need to be introduced to measure the similarity between the simulated and reconstructed sources. The well-known evaluation metrics are root mean square error (*RMSE*), shift of the maximum (S_{max}), shift of the center of mass (S_{cm}), and the correlation coefficient (*CC*) [51, 52]. Each metric has its own advantages and disadvantages. In contrast to the conventional geometric error metrics such as S_{max}, S_{cm} and DF, *RMSE* and *CC* do not reflect the geometry of the cortical surface. However, compared to S_{max}, S_{cm} and DF, *RMSE* and *CC* are reliable specifically when the source distributions are not concentrated to a single peak and several cluster of sources are existed. For more accurate and robust estimation of the accuracy of reconstructed EEG/MEG sources, we modified *CC* by giving the geodesic distance weights to the reconstructed sources to reflect the geometric information of cortical surface. To validate the new evaluation metric, named weighted correlation coefficient (*WCC*), some representative examples were used [53].

We assume that both the simulated true sources $\mathbf{j}$ and the estimated sources $\tilde{\mathbf{j}}$ are

distributed on the 3D cortical surface. We firstly summarize four conventional evaluation metrics, having been frequently used for assessing the accuracy of the source estimates.

4.2.1. Root Mean Square Error

The root mean square error (*RMSE*) is the most well-known and convenient way to measure the error between the actual source and the estimated source. *RMSE* is formulated as

$$RMSE = \sqrt{\frac{1}{n}\sum_{i=1}^{n}\left(j_i - \tilde{j}_i\right)^2}, \tag{4.1}$$

where j_i and $\tilde{j}_i$ are the i-th elements of $\mathbf{j}$ and $\tilde{\mathbf{j}}$ respectively.

This metric is easy to implement and can be used regardless of the shapes of the source distributions. However, *RMSE* does not reflect the geometry of the cortical surface since *RMSE* is computed with just vectored values.

4.2.2. Shift of the Maximum

The shift of the maximum (S_{max}) is the simplest measure which reflects the geometry of the source space. S_{max} indicates the distance between the locations where the maximum intensities of sources are generated. The maximum intensities of the actual and reconstructed source are assumed to be located at $\mathbf{r}_{\mathbf{max}}$ and $\tilde{\mathbf{r}}_{\mathbf{max}}$ respectively,

$$\mathbf{r_{max}} = \max_{\mathbf{r_i}}(j_i), \quad \tilde{\mathbf{r}}_{\mathbf{max}} = \max_{\mathbf{r_i}}(\tilde{j}_i), \tag{4.2}$$

where r_i is the coordinate of i-th node, then S_{max} is defined as

$$S_{max} = \sqrt{(\mathbf{r_{max}} - \tilde{\mathbf{r}}_{\mathbf{max}})^2}\ , \tag{4.3}$$

and ranged from 0 to d_{max}, the maximum distance within the brain.

This measure is reliable only when the actual source is concentrated around the location of the maximum source intensity because it does not consider the distributions of the cortical sources. When S_{max} is adopted as a measure, the merit of distributed source modeling disappears. For example, even when the extents of the true source and the reconstructed sources are largely different, identical maximum location makes the S_{max} value be 0.

4.2.3. Shift of the Center of Mass

The center of mass has been widely used for evaluating various algorithms adopted not only in EEG and MEG but also other functional brain imaging techniques such as functional magnetic resonance imaging (fMRI) and positron emission tomography (PET). The center of mass of the actual source $\mathbf{r_{cm}}$ and the center of mass of the reconstructed source $\tilde{\mathbf{r}}_{\mathbf{cm}}$ are computed as

$$\mathbf{r_{cm}} = \frac{\sum_{i=1}^{n} j_i \mathbf{r_i}}{\sum_{i=1}^{n} j_i}, \quad \tilde{\mathbf{r}}_{\mathbf{cm}} = \frac{\sum_{i=1}^{n} \tilde{j}_i \mathbf{r_i}}{\sum_{i=1}^{n} \tilde{j}_i}. \tag{4.4}$$

As assuming the distributed source to be a dipole source placed on the center of

mass of the source, the shift of center of mass (S_{cm}) is defined as the distance between $\mathbf{r_{cm}}$ and $\tilde{\mathbf{r}}_{\mathbf{cm}}$

$$S_{cm} = \sqrt{\left(\mathbf{r_{cm}} - \tilde{\mathbf{r}}_{\mathbf{cm}}\right)^2}. \tag{4.5}$$

S_{cm} is similar to S_{max} in that the distributed source is considered as a point source placed at a single location. Therefore, S_{cm} is also reliable only when the simulated source is concentrated around $\mathbf{r_{cm}}$. If the distribution of the source has a radial symmetry, S_{cm} becomes equivalent to S_{max}.

4.2.4. Degrees of Focalization

We assessed the accuracy of source estimation using the criterion called degrees of focalization (DF), which quantifies how much of the reconstructed source is contained in the reference source patch [45]. This validation metric was defined as follows and ranged in value from 0 to 100:

$$DF = \frac{\sum_{i \in \Pi} \hat{J}_i^2}{\sum_{i \in \Omega} \hat{J}_i^2} \times 100(\%), \tag{4.6}$$

where Ω denotes the whole source space and Π denotes the reference source patch. When the reconstructed source is distributed containing the actual source region, DF evaluates the accuracy of reconstruction well. However, When the reconstructed sources are concentrated in the region of actual source, the DF values are always 100.

4.2.5. Correlation Coefficient

The correlation coefficient (*CC*), a concept adopted from statistics, is a measure of linear dependency between two variables, and the value ranges between -1 and 1. It has been widely employed as a standard measure in various fields of engineering and sciences. The conventional CC is defined as the covariance of $\mathbf{j}$ and $\tilde{\mathbf{j}}$ divided by the product of their standard deviations:

$$CC = \frac{\mathrm{cov}(\mathbf{j}, \tilde{\mathbf{j}})}{\sqrt{\mathrm{cov}(\mathbf{j}, \mathbf{j})\,\mathrm{cov}(\tilde{\mathbf{j}}, \tilde{\mathbf{j}})}} \quad , \tag{4.7}$$

where the covariance is defined as

$$\mathrm{cov}(\mathbf{j}, \tilde{\mathbf{j}}) = \frac{1}{n}\sum_{i=1}^{n}(j_i - j^*)(\tilde{j}_i - \tilde{j}^*), \tag{4.8}$$

and j^* represents the mean value of the source $\mathbf{j}$:

$$j^* = \frac{1}{n}\sum_{i=1}^{n} j_i, \quad \tilde{j}^* = \frac{1}{n}\sum_{i=1}^{n} \tilde{j}_i. \tag{4.9}$$

If the distribution of the reconstructed sources is similar to that of the actual sources, the value of *CC* is close to 1; if the distribution of the reconstructed sources is different from that of the actual sources, *CC* is close to -1. *CC* is reliable even when the source distribution is not concentrated to a single location or when the true source has many distinct peaks. However, similar to *RMSE*, *CC* cannot reflect the real geometry of the cortical surface.

4.2.6. Weighted Correlation Coefficient

To combine the advantages of both geodesic and statistic conventional measures, we modified *CC* by giving the source vector a weight reflecting geometrical information of cortical surface. The new evaluation measure, named weighted correlation coefficient (*WCC*), is defined as

$$WCC = \frac{\mathrm{cov}(\boldsymbol{W}\mathbf{j}, \boldsymbol{W}\tilde{\mathbf{j}})}{\sqrt{\mathrm{cov}(\boldsymbol{W}\mathbf{j}, \boldsymbol{W}\mathbf{j})\,\mathrm{cov}(\boldsymbol{W}\tilde{\mathbf{j}}, \boldsymbol{W}\tilde{\mathbf{j}})}}. \tag{4.10}$$

and $\boldsymbol{W}$ is an n by n weighting matrix that can be computed as

$$\boldsymbol{W} = \frac{d_{\max}\boldsymbol{I_n} - \boldsymbol{D}}{d_{\max}}, \tag{4.11}$$

where $\boldsymbol{I_n}$ is an n by n identity matrix. $\boldsymbol{D}$ is an n by n distance matrix whose element is given as

$$D_{ij} = \left\| \mathbf{r_i} - \mathbf{r_j} \right\|_k, \tag{4.12}$$

and d_{max} is the maximum value in $\boldsymbol{D}$. If k=2, the Euclidean distance is employed and if k=geo then the geodesic distance is employed to obtain the distance matrix. The geodesic distance was computed by solving the Eikonal equation on the tessellated cortical surface [54]. The main diagonal of the weight matrix $\boldsymbol{W}$ was filled with 1 and the off-diagonal elements were filled with values between 0 and 1. By multiplying weight matrix $\boldsymbol{W}$ to the source vector $\mathbf{j}$, the geometric information of cortical surface is considered.

Additionally, Euclidean or geodesic distance can be employed in the definition of the distance matrix $\boldsymbol{D}$. Since the cortical surface of a human brain is folded, the

geodesic distance is more suitable to reflect the geometric information of the cortical surface than the Euclidean distance. The Euclidian distance is computed by the Cartesian coordinates regardless of the geometrical feature of the cortical surface. However, as the geodesic distance implies the minimum distance along the surface, the geodesic distance between the two adjacent gyri should be greater than the Euclidian distance. Figure 4.1 is an example of the Euclidean and geodesic distance between each cortical surface vertex and a reference point located at right dorsolateral prefrontal cortex, corresponding to a column of the distance matrix.

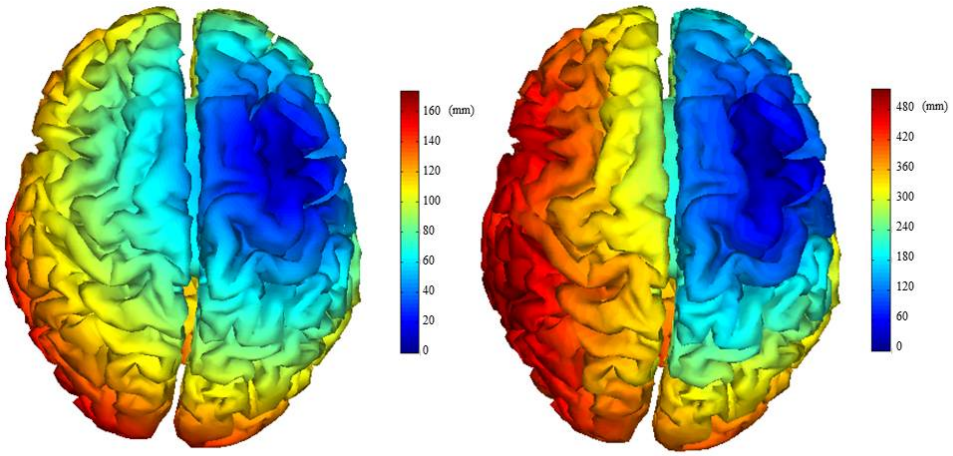

Figure 4.2. one column of (a) Euclidean and (b) Geodesic distance matrix visualized on the cortical surface

The characteristics of the conventional and proposed measures are summarized in Table 1. Low values of *RMSE*, S_{max} or S_{cm} and high values of *CC* and *WCC* indicate the accurate reconstruction. Only *WCC* is applicable to the case of multi peak and can consider the geometry of source space.

Table 4.1. The merits and demerits of measures

measures	reflection of geometry	multiple peaks	bound	unit
RMSE	no	yes	0~∞	no unit
S_{max}	yes	no	0~d_{max}	*mm*
S_{cm}	yes	no	0~ d_{max}	*mm*
DF	no	no	0~1	no unit
CC	no	yes	-1~1	no unit
WCC	yes	yes	-1~1	no unit

To compare and verify the conventional and proposed measures, a simple two-dimensional example was simulated as shown in Figure 4.3. The source space was defined as a two-dimensional rectangle. The actual source distribution $\mathbf{x}$ is given in Figure 4.3 (a) and five reconstructed sources are given in Figures 4.3 (b)-(f), each of which was denoted as $\mathbf{y_1}$, $\mathbf{y_2}$, $\mathbf{y_3}$, $\mathbf{y_4}$ and $\mathbf{y_5}$. The source current intensities are indicated with different colors. If we evaluate the reconstructed sources based on visual inspection, anyone would agree that $\mathbf{y_1}$ is the most accurate reconstruction and $\mathbf{y_2}$ is the second best one. $\mathbf{y_5}$ seems to be the worst reconstruction as the peak location is farthest from the actual one and no reconstructed source is overlapped with the

actual one. $\mathbf{y_3}$ and $\mathbf{y_4}$ seems to be better matched than $\mathbf{y_5}$ but it is difficult to judge which result is better. The result $\mathbf{y_3}$ has no commonly activated region with the actual source but the distribution is close to the actual source distribution; whereas $\mathbf{y_4}$ has slightly overlapped region but other regions are located far from the actual source location. If we assume visual inspection (*VI*) as a qualitative measure, the rank of the reconstructed sources can be expressed as $VI(\mathbf{x},\mathbf{y_1}) > VI(\mathbf{x},\mathbf{y_2}) > VI(\mathbf{x},\mathbf{y_3}) \geq VI(\mathbf{x},\mathbf{y_4}) > VI(\mathbf{x},\mathbf{y_5})$.

We then employed the conventional and proposed quantitative measures for the evaluation of the reconstructions depicted in Figure 4.3 and summarized the result in Table 4.2. All measures commonly indicated that $\mathbf{y_1}$ is the best reconstruction and $\mathbf{y_5}$ is the worst reconstruction. However, the different metrics showed different evaluation results for $\mathbf{y_2}$, $\mathbf{y_3}$ and $\mathbf{y_4}$. In the case of *RMSE*, $\mathbf{y_3}$ was evaluated as the worst reconstruction and $\mathbf{y_4}$ and $\mathbf{y_2}$ had an identical *RMSE* value, which was because *RMSE* was affected by the commonly activated regions regardless of the source geometry. In the case of S_{max}, which considers only the maximum location of the source, the results of $\mathbf{y_2}$ and $\mathbf{y_4}$ were equivalent. Similar to *RMSE*, *CC* classified $\mathbf{y_3}$ as the worst reconstruction and $\mathbf{y_4}$ and $\mathbf{y_2}$ had an identical *CC* value. Both S_{cm} and *WCC* evaluated the reconstruction results identically to the visual inspection results. However, if the actual source has multiple peaks, S_{cm} cannot be accurately evaluated.

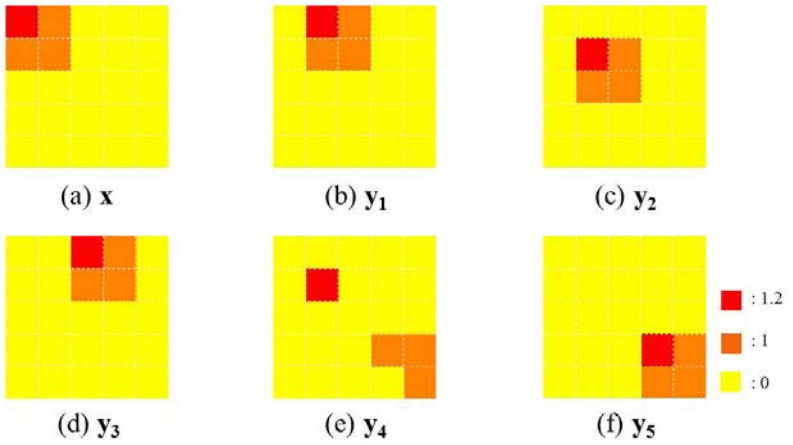

Figure 4.3. Example of a simulated two dimensional source space : (a) the actual source distribution (b)-(f) the reconstructed sources

Table 4.2. Evaluation of reconstructions depicted in Figure 4.3

	$\mathbf{y}_1$	$\mathbf{y}_2$	$\mathbf{y}_3$	$\mathbf{y}_4$	$\mathbf{y}_5$
RMSE	2.12	2.53	2.98	2.73	2.98
S_{max}	1.00	1.41	2.00	1.41	4.24
S_{cm}	1.00	1.41	2.00	2.87	4.24
DF	52.38	28.57	0.00	28.57	0.00
CC	0.40	0.13	-0.19	0.25	-0.19
WCC	0.89	0.80	0.48	-0.31	-0.79

5. Algorithm Considering the Directional Characteristics

5.1 Proposed Algorithm

Our goal in the chapter is to develop a new multimodal source imaging algorithm that can integrate simultaneously recorded EEG and MEG data to enhance overall localization accuracy, even under circumstances in which a specific directional component of the neuronal source is dominant. To account for the different directional sensitivities of EEG and MEG, we decomposed the sensor and source spaces into radial and tangential components conceptually and developed a new explicit formulation to solve the inverse problem.

While trivial in a spherical head model, the radial directions of cortical sources in a realistic geometric head model need to be defined differently. In the present study, the radial direction **r** of a cortical source was defined as the orientation along which the total magnetic flux density generated by a unit dipole placed at a source location is minimized. To identify the radial direction, singular value decomposition (SVD) was applied to the MEG leadfield matrix and the singular vector corresponding to the weakest singular value was assigned to the radial directional vector [55]. Because the cortical current is generally assumed to be oriented perpendicularly to the cortical surface, the unit normal directional vector **n** can be explicitly defined at every location on the cortical surface. Using the Gram-Schmidt orthogonal process, the

tangential direction **t** at the *i*-th cortical vertex ($1 \le i \le m$) can be uniquely determined as

$$\mathbf{t}(i) = \mathbf{n}(i) - \frac{\langle \mathbf{n}(i), \mathbf{r}(i) \rangle}{\|\mathbf{r}(i)\|^2} \mathbf{r}(i), \tag{5.1}$$

where <**x**, **y**> denotes the inner product of the two vectors **x** and **y,** ||**x**|| denotes the Euclidian norm of the vector **x**, indices in parentheses represent the vertex number, and *m* is the number of cortical vertices.

After evaluating the tangential, radial, and normal directions at every cortical vertex, we define *m* by *m* diagonal matrices P_t and P_r, whose (*i*, *i*)-th elements represent the ratios of tangential and radial components to the normal component of the *i*-th cortical source, respectively, that is

$$P_t(i, j) = \begin{cases} \dfrac{\langle \mathbf{n}(i), \mathbf{t}(i) \rangle}{\|\mathbf{t}(i)\|^2}, & \text{if} \quad i = j \\ 0, & \text{if} \quad i \neq j \end{cases} \tag{5.2}$$

and

$$P_r(i, j) = \begin{cases} \dfrac{\langle \mathbf{n}(i), \mathbf{r}(i) \rangle}{\|\mathbf{r}(i)\|^2}, & if \quad i = j \\ 0, & if \quad i \neq j \end{cases} \tag{5.3}$$

for each $1 \le i, j \le m$. Then, P_t and P_r satisfy

$$P_t^2 + P_r^2 = I, \tag{5.4}$$

where *I* denotes an identity matrix of order *m*.

In the source space, the cortical source $\mathbf{j} = [j_1, j_2, \ldots, j_i, \ldots, j_m]^T$, oriented perpendicularly to the cortical surface, can be decomposed into tangential source

components $\mathbf{j_t} = [j_{t,1}, j_{t,2},\ldots, j_{t,i},\ldots, j_{t,m}]^T$ and radial source components $\mathbf{j_r} = [j_{r,1}, j_{r,2},\ldots, j_{r,i},\ldots, j_{r,m}]^T$ using P_t and P_r, in the form of

$$\begin{aligned} \mathbf{j_t} &= P_t\mathbf{j}, \\ \mathbf{j_r} &= P_r\mathbf{j}. \end{aligned} \tag{5.5}$$

Using (5.4) and (5.5), the cortical sources can be rewritten as

$$\mathbf{j} = I\mathbf{j} = (P_t^2 + P_r^2)\mathbf{j} = P_t(P_t\mathbf{j}) + P_r(P_r\mathbf{j}) = P_t\mathbf{j_t} + P_r\mathbf{j_r}. \tag{5.6}$$

The leadfield matrices corresponding to EEG and MEG project the source space to the sensor space so that

$$\begin{aligned} \mathbf{v} &= K_{eeg}\mathbf{j}, \\ \mathbf{b} &= K_{meg}\mathbf{j}, \end{aligned} \tag{5.7}$$

where $\mathbf{v}$ represents the electric potential recorded at scalp electrodes, $\mathbf{b}$ represents the magnetic flux density recorded at SQUID sensors, and K_{eeg} and K_{meg} represent the leadfield matrices of EEG and MEG, respectively, each of which can be obtained by solving EEG and MEG forward problems.

In the sensor space, the electric potential $\mathbf{v}$ at the scalp EEG sensors is conceptually decomposed into $\mathbf{v_t}$ and $\mathbf{v_r}$, which are generated by $\mathbf{j_t}$ and $\mathbf{j_r}$, respectively, and the magnetic flux density $\mathbf{b}$ passing through MEG sensors is also decomposed into $\mathbf{b_t}$ and $\mathbf{b_r}$, generated by $\mathbf{j_t}$ and $\mathbf{j_r}$, respectively; that is

$$\begin{aligned} \mathbf{v} &= \mathbf{v_t} + \mathbf{v_r}, \\ \mathbf{b} &= \mathbf{b_t} + \mathbf{b_r}. \end{aligned} \tag{5.8}$$

Then, the relations between sources and the directional components of $\mathbf{v}$ and $\mathbf{b}$ can be described as

$$\begin{aligned} \mathbf{v_t} &= K_{t,eeg}\mathbf{j_t},\ \mathbf{v_r} = K_{r,eeg}\mathbf{j_r}, \\ \mathbf{b_t} &= K_{t,meg}\mathbf{j_t},\mathbf{b_r} = K_{r,meg}\mathbf{j_r}, \end{aligned} \tag{5.9}$$

where the directional leadfield matrices, $K_{t,eeg}$, $K_{r,eeg}$, $K_{t,meg}$, and $K_{r,meg}$ have the following relationships:

$$\begin{aligned} K_{t,eeg} &= K_{eeg}P_t, \\ K_{r,eeg} &= K_{eeg}P_r, \\ K_{t,meg} &= K_{meg}P_t, \\ K_{r,meg} &= K_{meg}P_r. \end{aligned} \tag{5.10}$$

When linear inverse estimation is applied, the tangential component of cortical sources $\hat{\mathbf{j}}_\mathbf{t}$ can be estimated using either

$$\hat{\mathbf{j}}_\mathbf{t} = G_{t,eeg}\mathbf{v_t} \tag{5.11}$$

or

$$\hat{\mathbf{j}}_\mathbf{t} = G_{t,meg}\mathbf{b_t}, \tag{5.12}$$

where $G_{t,eeg}$ and $G_{t,meg}$ represent the *tangential* inverse operators with respect to EEG and MEG, respectively. Similarly, the radial components of cortical sources $\hat{\mathbf{j}}_\mathbf{r}$ can be estimated using either

$$\hat{\mathbf{j}}_\mathbf{r} = G_{r,eeg}\mathbf{v_r}, \tag{5.13}$$

or

$$\hat{\mathbf{j}}_\mathbf{r} = G_{r,meg}\mathbf{b_r}, \tag{5.14}$$

where $G_{r,eeg}$ and $G_{r,meg}$ represent the radial inverse operators of EEG and MEG, respectively. The derivations of the directional inverse operators are provided in the Appendix B.

We consider the decomposition of the estimated source $\hat{\mathbf{j}}$. Similarly to (5.5) and (5.6), the estimated source $\hat{\mathbf{j}}$ can also be decomposed into tangential and radial components; that is,

$$\begin{aligned}\hat{\mathbf{j}} &= P_t{}^2\hat{\mathbf{j}} + P_r{}^2\hat{\mathbf{j}} \\ &= P_t\hat{\mathbf{j}}_\mathbf{t} + P_r\hat{\mathbf{j}}_\mathbf{r}.\end{aligned} \tag{5.15}$$

The tangential component $\hat{\mathbf{j}}_\mathbf{t}$ was estimated from (5.12) and the radial component $\hat{\mathbf{j}}_\mathbf{r}$ was estimated from (5.13). Substituting (5.12) and (5.13) into (5.15) gives

$$\hat{\mathbf{j}} = P_tG_{t,meg}\mathbf{b}_\mathbf{t} + P_rG_{r,eeg}\mathbf{v}_\mathbf{r}, \tag{5.16}$$

and applying (5.5) and (5.9) to (5.16) gives

$$\hat{\mathbf{j}} = P_tG_{t,meg}K_{t,meg}P_t\mathbf{j} + P_rG_{r,eeg}K_{r,eeg}P_r\mathbf{j}. \tag{5.17}$$

When define the error between the exact and reconstructed sources $\mathbf{e}$ as

$$\mathbf{e} = \mathbf{j} - \hat{\mathbf{j}}, \tag{5.18}$$

we can rewrite (5.17) as

$$\mathbf{j} = P_tG_{t,meg}K_{t,meg}P_t\mathbf{j} + P_rG_{r,eeg}K_{r,eeg}P_r\mathbf{j} + \mathbf{e}. \tag{5.19}$$

Rearranging (5.19),

$$\mathbf{e} = \left\{I - P_tG_{t,meg}K_{t,meg}P_t - P_rG_{r,eeg}K_{r,eeg}P_r\right\}\mathrm{j} := Q\mathbf{j}, \tag{5.20}$$

where $Q = I - P_tG_{t,meg}K_{t,meg}P_t - P_rG_{r,eeg}K_{r,eeg}P_r$.

Now, we consider a general constrained minimization problem for weighted minimum norm estimation (WMNE) [56],

$$\min_{\mathbf{j}} \|\mathbf{j}\|_W^2, \text{ subject to } \mathbf{y} = K\mathbf{j}, \tag{5.21}$$

where W represents the source weighting matrix and

$$\|\mathbf{j}\|_W^2 := \mathbf{j}^T W \mathbf{j}. \tag{5.22}$$

Then, the solution of (5.21) $\tilde{\mathbf{j}}$ is known to be

$$\tilde{\mathbf{j}} = W^{-1} K^T \left[K W^{-1} K^T \right]^{-1} \mathbf{y}. \tag{5.23}$$

In our problem, we need to minimize the error between the exact and reconstructed sources **e**, defined in (5.18); thus the definition of our problem becomes

$$\min_{\mathbf{j}} \|\mathbf{e}\|_2, \text{ subject to } \mathbf{y} = K\mathbf{j}. \tag{5.24}$$

In our problem, **y** represents the combined EEG and MEG data $\mathbf{y} = \begin{bmatrix} \mathbf{b} \\ \mathbf{v} \end{bmatrix}$, K represents the combined leadfield matrix $K = \begin{bmatrix} K_{meg} \\ K_{eeg} \end{bmatrix}$ and **j** is the source strength that we need to estimate. In the linear equation $\mathbf{y} = K\mathbf{j}$, each of the leadfield matrices of EEG and MEG as well as each of the EEG and MEG signal datasets are normalized so that the elements in the combined leadfield matrix equation have equivalent orders [57-65]. To accomplish this, the leadfield matrices of EEG and MEG (K_{eeg} and K_{meg}) are first normalized by the matrix norms of EEG and MEG, respectively. Then, the same scale factors are applied to the EEG and MEG signal data (**v** and **b**), respectively. The normalized leadfield matrices and data sets are then stacked into a single leadfield matrix K and a data vector **y**.

If set the source weighting matrix W in (5.21) to

$$W := Q^T Q, \tag{5.25}$$

we can transform the general WMNE problem in (3.38) into our problem in (5.24), because the equation (5.22) becomes

$$\|\mathbf{j}\|_W^2 = \mathbf{j}^T W \mathbf{j} = (Q\mathbf{j})^T Q\mathbf{j} = \mathbf{e}^T \mathbf{e} = \|\mathbf{e}\|^2. \tag{5.26}$$

Then, we can directly utilize the known solution of WMNE written in (5.23). Thus, the solution of our problem given in (5.24) can be found by substituting (5.25) into (5.23):

$$\tilde{\mathbf{j}} = \left(Q^T Q\right)^{-1} K^T \left[K\left(Q^T Q\right)^{-1} K^T\right]^{-1} \mathbf{y}, \tag{5.27}$$

where

$$Q = I - P_t G_{t,meg} K_{t,meg} P_t - P_r G_{r,eeg} K_{r,eeg} P_r. \tag{5.28}$$

When additive noise is present in the signals, a regularization term needs to be introduced. Then the expression for the solution becomes

$$\tilde{\mathbf{j}} = \left(Q^T Q\right)^{-1} K^T \left[K\left(Q^T Q\right)^{-1} K^T + \lambda I\right]^{-1} \mathbf{y}, \tag{5.29}$$

where λ is a regularization parameter and was determined using the generalized cross validation method [66]. Note that the notation $\hat{\mathbf{j}}$ is a dummy variable used only to construct the source weighting matrix W during the formulation, and $\tilde{\mathbf{j}}$ denoted in (5.27) is the final source estimate [67].

5.2 Numerical Experiment of Proposed Method

To further investigate the influence of the orientations of the cortical sources on localization accuracy, the 4,568 source patches were classified on the basis of the proportion of the radial component γ, defined as

$$\gamma = \sum_{i \in \Pi} \frac{j_{r,i}^2}{j_i^2}, \tag{5.30}$$

where Π denotes the source patch area, i represents the i-th cortical vertex, $j_{r,i}$ is the amplitude of the radial component of a cortical source at the i-th vertex, and γ ranges from 0 to 1. A value of γ close to 0 indicates that a cortical source patch is oriented in the tangential direction, whereas a value of γ close to 1 indicates that a source patch is oriented in the radial direction. The histogram depicted in Figure 5.1 shows the distribution of the number of source patches with respect to γ with a bin size of 0.05. From this figure, it is clear that more cortical sources are oriented in a tangential direction than are oriented in a radial direction. Because the number of source patches whose γ value exceeding 0.8 was not sufficient to estimate average localization accuracies, which was smaller than a third of the smallest number of source patches in a single bin in which the γ value was less than 0.8, we excluded those patches when analyzing the simulation results shown in Figure 5.3.

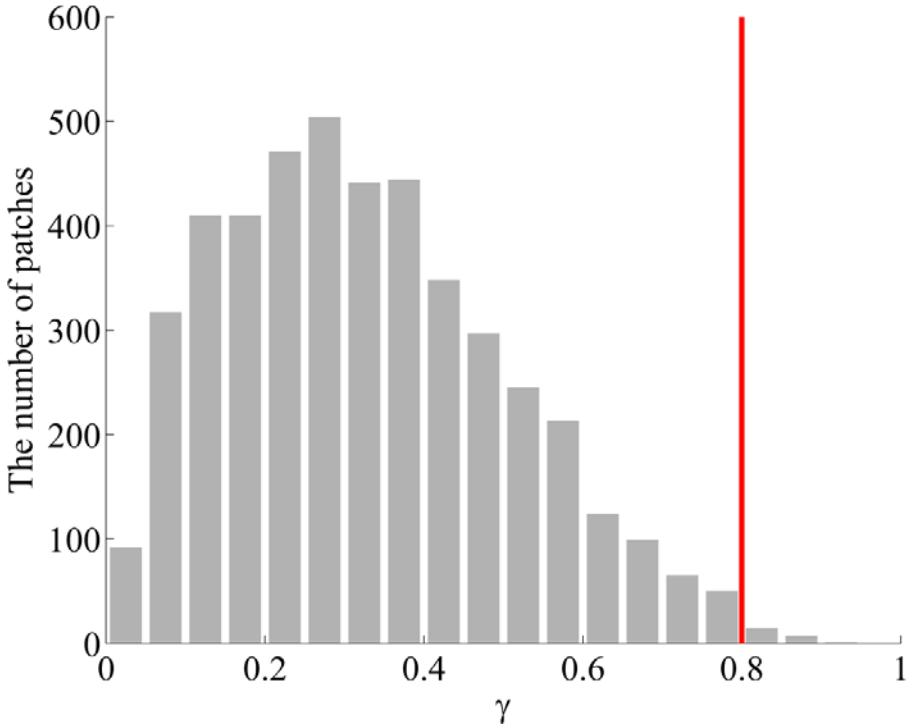

Figure 5.1. Distribution of cortical source patches with respect to the proportion of the radial component of sources.

We first evaluated source localization accuracies for four different cases: 1) source imaging with only EEG data (*EEG alone* case); 2) source imaging with only MEG data (*MEG alone* case); 3) source imaging using conventional integration method based on a simple order normalization to combine the EEG and MEG data sets (conventional method); and 4) source imaging using the proposed multimodal integration method (proposed method) shown in Figure 5.2.

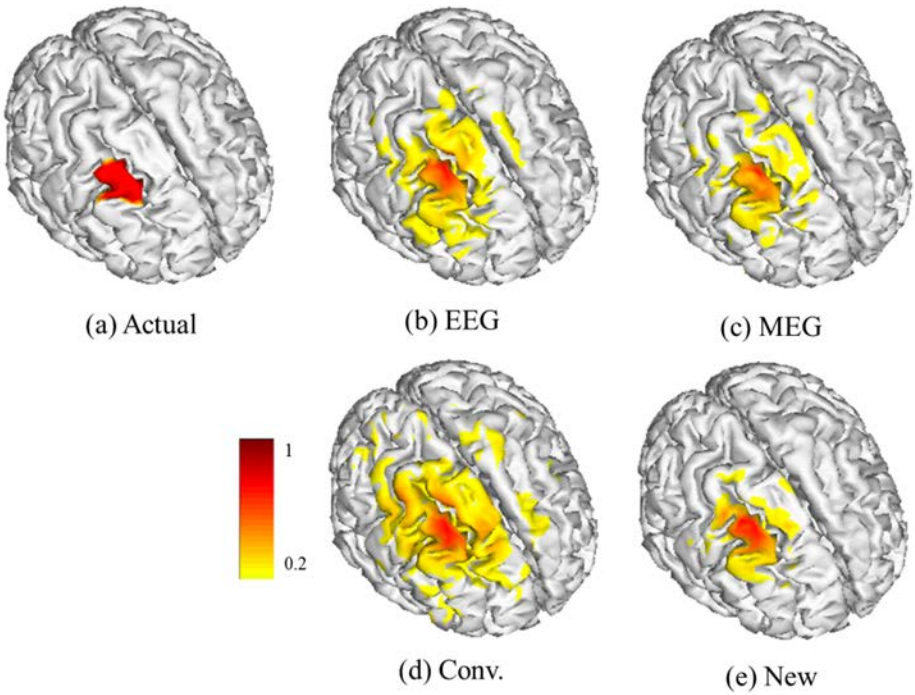

Figure 5.2. (a) The simulated actual source and the corresponding reconstructed results using different methods, (b) EEG, (c) MEG, (d) conventional combined method and (d) Proposed combined method

We reconstructed cortical source distributions using the EEG/MEG forward data sets simulated for each of the 4,568 cortical patches. White Gaussian noise was added to the simulated EEG and MEG signals. We set the signal-to-noise ratio (SNR) values of EEG and MEG to 10 and 30, respectively, considering that EEG data generally contains more noise than MEG data in practice when the SNR values were defined as ten times of the log-scaled square root of the ratio of the simulated signal power to the noise power. The variations in the DF values averaged in each bin with respect to the proportion of the radial component (γ) values are shown in Figure 5.3. The localization accuracy of the *EEG alone* case increased and that of the *MEG alone* case decreased as the γ value increased, demonstrating that EEG and MEG source localization results are dependent upon the source orientations when constant background noise is added to the neural electrical signals. These results indicate that MEG is better than EEG at estimating tangential sources whereas EEG is better than MEG at estimating radial sources.

The conventional method generally yielded more accurate source estimation results than either *EEG alone* or *MEG alone* cases, but it did not always enhance localization accuracy, particularly when the radial source component was dominant ($\gamma > 0.6$). In contrast, our *proposed method* enhanced the localization accuracy for every γ value and moreover, resulted in a significant improvement in localization accuracy, particularly when either the radial or tangential components of the cortical sources were dominant.

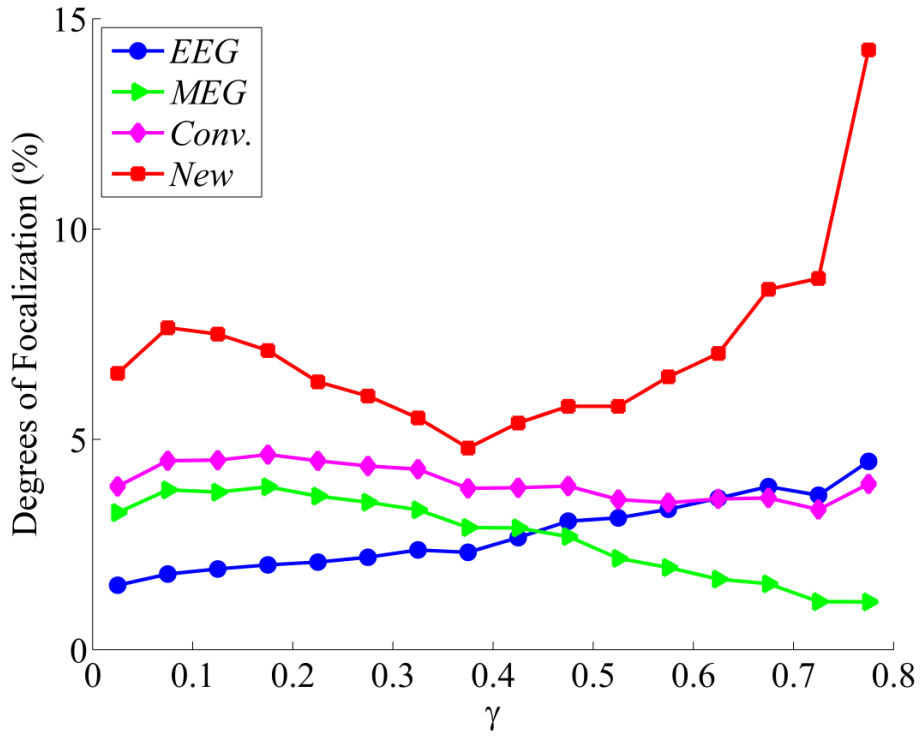

Figure 5.3. Average localization accuracies in four cases with respect to the proportion of the radial component: (case A) Cortical sources estimated with EEG data alone; (case B) Cortical sources estimated with MEG data alone; (case C) The conventional combined EEG-MEG source estimation method was applied; (case D) The proposed EEG-MEG integration method was applied.

The spatial distributions of the DF values measured at each cortical source patch for the four cases listed above are shown in Figure 5.4; the DF value of the source patch was assigned to the center of the patch. Figure 5.4 (a) and (b) show that the *EEG alone* and *MEG alone* cases provided relatively more accurate source estimates only around some specific cortical areas. Interestingly, the cortical areas with high DF values in the *EEG alone* case (Figure 5.4 (a)) and the *MEG alone* case (Figure 5.4(b)) were separated and complementary to each other. In contrast, the *conventional method* enhanced the localization accuracy in cortical areas in which either the *EEG alone* or *MEG alone* cases could not accurately reconstruct source distributions (Figure 5.4 (c)). However, the enhancement in the absolute DF values was comparable to those obtained from either of the two modalities, showing that an additional synergy effect was not obtainable using the conventional approach. In contrast, our proposed method showed significantly enhanced localization accuracy compared to that of the conventional integration method (see Figure 5.4 (d)).

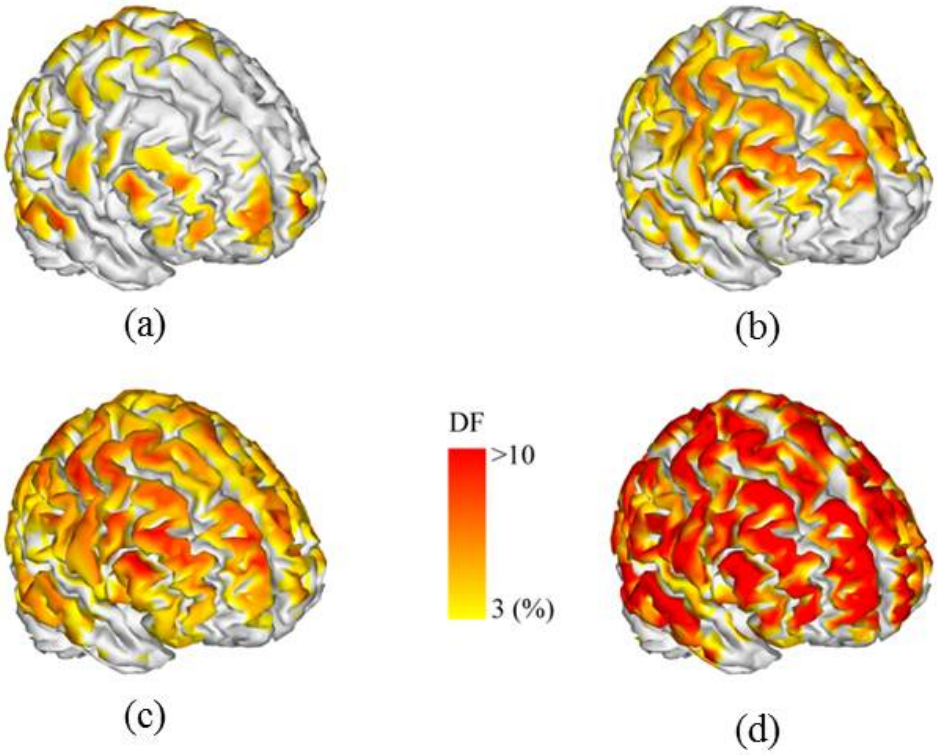

Figure 5.4. Localization accuracy of four cases mapped on the cortical surface: (A) EEG method; (B) MEG method; (C) conventional integration method; (D) proposed integration method. The color code indicates the DF value assigned at the center of each reference source patch. The color map of the DF value was thresholded at 3%.

6. Algorithm Considering the Maximum Current Density

6.1 Proposed Algorithm

The MNE algorithm is one of the earliest algorithms developed for cortical source imaging and is based on the L2 norm minimization. The general form of the function to be minimized can be expressed as

$$\min_{\mathbf{j}} \left\| \mathbf{j} \right\|_2 , \text{ subject to } \mathbf{b} = K\,\mathbf{j} , \tag{6.1}$$

where K is an m by n leadfield matrix that relates m sensors and n sources, $\boldsymbol{j}$ is an n by 1 vector representing the strength of n sources. The general MNE solution can be expressed in the form of linear equations and thus can be readily obtained without any iterative processes. The MNE solution is usually diffused over the whole cortical surface.

The reconstructed source with MCE adapts L1 norm minimization as

$$\min_{\mathbf{j}} \left\| \mathbf{j} \right\|_1 , \text{ subject to } \mathbf{b} = K\,\mathbf{j} , \tag{6.2}$$

and the MCE solution is usually concentrated to the center of the source compared to that with MNE.

To estimate the distribution of the source as well, we employ additional constraint term of maximum bound of source amplitude to the minimization problem:

$$\min_{\mathbf{j}} \left\| \mathbf{j} \right\|_1 , \text{ subject to } \mathbf{b} = K\,\mathbf{j} \;\; \& \;\; \left| j_i \right| \le p, \tag{6.3}$$

where p denotes the estimated maximum bound of current source. The proposed method is named as bounded minimum current estimate (BMCE). The conversion process to general form of linear programming (LP) is able to solve this minimum problem efficiently [48, 68-76]. In the simulation, Open source linear programming system, *LP solve* [77] based on the revised simplex method and the Branch and bound method is applied to solve (6.3).

And the maximum bound of current source (p) can be estimated by L-curve analysis of L1 norm of reconstructed source against the values p and the process is explained in chapter 6.2.

Moreover the additional constraint term of maximum bound of source amplitude also can be combined to the weighting algorithm proposed in chapter 5. Then the constraint minimum norm problem becomes

$$\min_{\mathbf{j}} \left\| W\mathbf{j} \right\|_1 , \text{ subject to } \mathbf{b} = K\,\mathbf{j} \quad \& \quad \left| j_i \right| \le p, \tag{6.4}$$

where the W is the matrix which is consisted by the directional characteristics of source, K is the combined leadfield matrix of EEG and MEG and $\mathbf{b}$ is combined EEG and MEG data.

6.2 Numerical Experiment of Proposed Method

The goal of the proposed method in Chapter 6.1 was to reconstruct the source regardless of the extension of the distribution. Motivated by general situation that the reconstructed source with MNE is blurred and the maximum current density (p_{MNE}) is small, contract to that with MCE is focal and the maximum current density (p_{MCE}) is much greater than that of actual source (p^*), we investigate the distribution of reconstructed sources as changing the maximum bound of BMCE (p) from p_{MNE} to p_{MCE}. Figure 6.1 shows the reconstructed source for various maximum bounds. We can observe that if the maximum bound is less than the actual bound, the source is weighed down to be distributed out of the actual patch. And source is getting focalized as the maximum bound increases. When the maximum bound is equal to the maximum of actual source, the reconstructed source is very close to the actual source distribution. And the source is getting focalized as the maximum bound approaches to p_{MCE}. If p is getting greater than p_{MCE}, the solution of MCE and BMCE is equivalent and the L1 norm of the BMCE solution becomes stabilized.

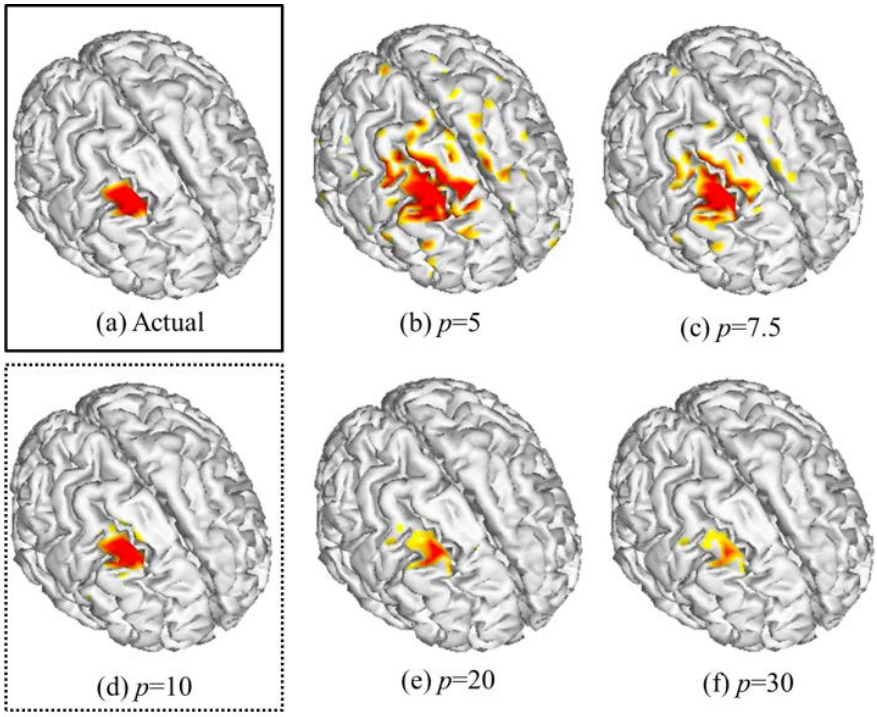

Figure 6.1. Reconstructed sources for various maximum bound

Therefore, in Figure 6.2 (a), we plotted a graph of maximum bound and L1 norm of the reconstructed source with the result of Figure 6.1. The graph is L-shaped and we expect the corner of graph to be the actual bound. The L-curve method for parameter selection is to pick the value corresponding to the “corner” of the L-curve. The curvature which indicate the degree of rapid change is defined as

$$k = \frac{|y''|}{(1+y'^2)^{3/2}}, \tag{6.5}$$

and usually employed in L-curve method [77-80]. Figure 6.2 (b) shows the curvature with respect to the maximum bound. We employ the maximum bound corresponding to the maximum curvature. In this case the estimated maximum bound for BMCE is decided to 9.6 and the actual bound was 10. Figure 6.2 (c) shows the evaluation metric *WCC* proposed in Chapter 4.2 with respect to the maximum bound. The accuracy of reconstructed source with the actual maximum bound is marked with a square and that with estimated maximum bound is marked with a disk.

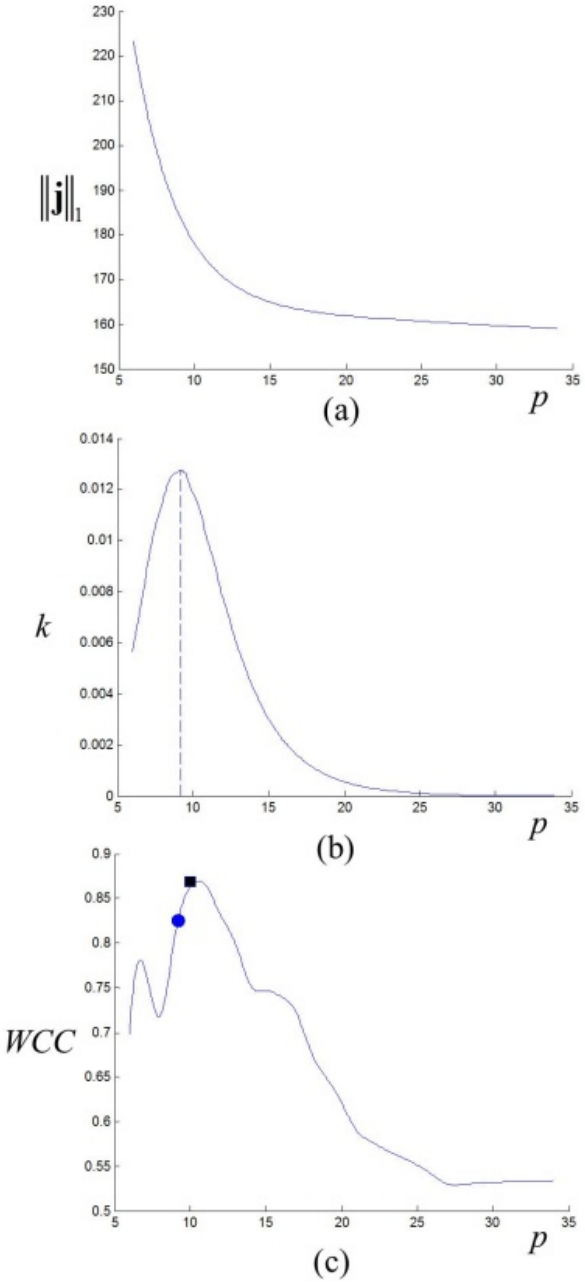

Figure 6.2. (a) The graph of the L1 norm of the reconstructed source with respect to the maximum bound (b) The curvature of (a) and dot line is the estimated maximum bound (c) *WCC* with respect to the maximum bound

In Figure 6.3, we show the comparison between MNE, MCE and BMCE for various source's area. The simulated current source is displayed in the first column of Figure 6.3. After solving the forward problem, each inverse algorithm reconstructed the distributed source. BMCE* and BMCE localize sources with the actual maximum bound and the estimated maximum bound respectively. The MNE produces overly diffuse source estimates because of the L2 norm constraint. MCE generates focal source estimate regardless of the distributed pattern of source due to the nature of the L1 norm constraint on the estimated source strength. On the other hand, the source estimate of BMCE can more accurately reconstruct the distribution of the simulated sources.

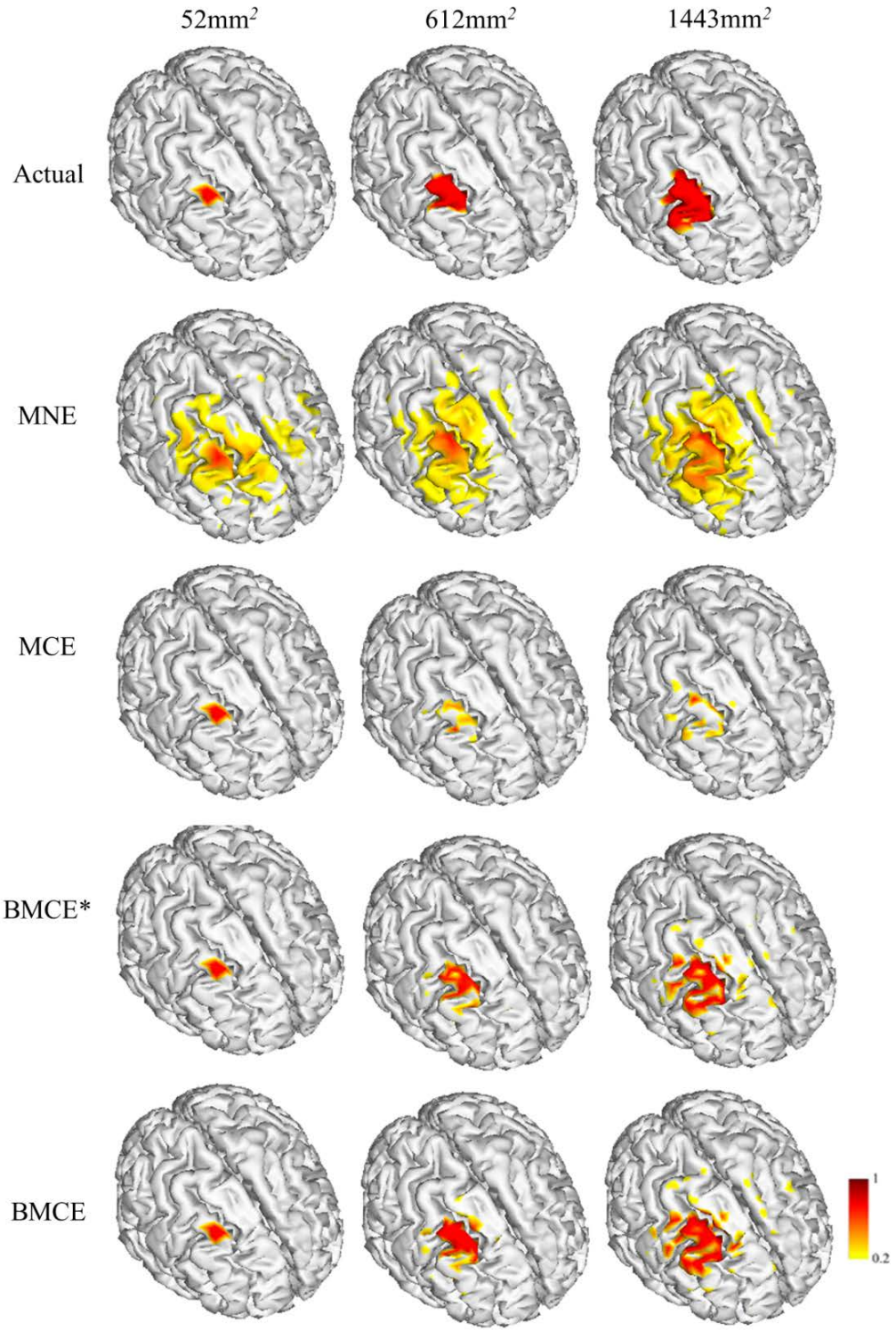

Figure 6.3. Comparison of conventional and proposed methods with various extensions of th e actual source area.

To further validate our hypothesis, we performed extensive computer simulation for 4,568 source locations on the cortical surface and quantified the improvement of the proposed method regardless of activated source area on the EEG source imaging. At each source location, four extended source patches with different areas were generated as shown in the previous example (Figure 6.3). The white Gaussian noise corresponded to 10% of the magnitude of the simulated EEG data are added.

Table 6.1 summarizes the result of massive simulation. Depending on the activated area, averaged values of *RMSE*, S_{max}, S_{cm}, *DF*, *CC* and *WCC* of reconstruction sources of conventional and proposed methods are presented. It could be readily observed from the table that MNE is accurate for the extended source and MCE is accurate for the focalized source. BMCE is much more accurate than two conventional methods regardless the extension of the source area. The intuitive and quantitative comparisons suggest that the proposed BMCE enhances the estimation accuracy.

Compared to MNE which computes directly the linear inverse operator, other methods based on the L1 minimum problem compute the solution iteratively by the revised simplex method [48]. In the view of computational time, MNE is very efficient and capable to be applied to the real time monitoring when the linear inverse operator is computed in advance. The computational time of MCE and BMCE is almost same. However, BMCE* is required additional process to estimate the maximum bound *p* which is ranged from the maximum of MCE and MNE and divided by 10 sections in this simulation. Therefore the BMCE* costs the 10 times

computational cost compared to the BMCE and MCE. The trade-off between the accuracy and computational time are existed for the proposed method.

Table 6.1. The result of massive simulation

area	method	*RMSE*	S_{max}	S_{cm}	*DF*	*CC*	*WCC*	*T (s)*
11.3 (mm^2)	MNE	15.91	5.14	17.4	21.15	0.53	0.66	0.12
	MCE	5.13	2.43	1.75	95.12	0.67	0.52	0.52
	BMCE*	1.56	2.52	1.32	97.93	0.74	0.84	0.51
	BMCE	1.63	2.65	1.55	96.24	0.73	0.83	5.12
69.6	MNE	22.44	6.45	15.03	43.4	0.83	0.87	0.12
	MCE	39.82	4.95	1.08	86.39	0.66	0.70	0.53
	BMCE*	14.88	4.36	0.95	88.8	0.90	0.92	0.52
	BMCE	20.01	4.44	1.03	88.4	0.84	0.91	5.22
689.12	MNE	34.35	6.53	14.54	40	0.85	0.89	0.12
	MCE	54.83	5.74	1.91	95	0.54	0.42	0.53
	BMCE*	13.14	4.27	1.74	91	0.89	0.91	0.54
	BMCE	15.25	4.47	1.41	93	0.87	0.91	5.42

Table 6.2 summarizes the result of massive simulation with respect to different noise levels. The averaged area of activated source is 69.6 mm^2. Depending on different noise levels, averaged values of *RMSE*, S_{max}, S_{cm}, *DF*, *CC* and *WCC* of reconstruction sources of conventional and proposed methods are presented. It could be readily observed from the BMCE is more accurate than conventional methods.

Table 6.2. The result of massive simulation with respect to the noise level

noise	method	*RMSE*	*Smax*	*Scm*	*DF*	*CC*	*WCC*	*T (s)*
10%	MNE	22.44	6.45	15.03	43.43	0.83	0.87	0.12
	MCE	39.82	4.95	1.08	86.39	0.66	0.70	0.53
	BMCE*	14.88	4.36	0.95	88.82	0.90	0.92	0.52
	BMCE	20.01	4.44	1.03	88.44	0.84	0.91	5.22
20%	MNE	25.37	6.90	15.90	40.41	0.73	0.80	0.12
	MCE	41.22	5.23	2.10	84.62	0.59	0.68	0.53
	BMCE*	15.18	4.61	1.14	86.84	0.88	0.88	0.52
	BMCE	16.11	4.82	1.33	83.53	0.81	0.87	5.22
30%	MNE	38.51	7.93	16.11	40.10	0.69	0.76	0.12
	MCE	55.11	6.34	2.51	80.52	0.54	0.60	0.53
	BMCE*	14.48	4.74	1.84	85.24	0.83	0.86	0.54
	BMCE	16.10	4.98	1.89	84.13	0.79	0.81	5.42

In Figure 6.4, we simulated the combination of compact and extended sources. Diffused MNE solution cannot reflect the focal source region and MCE solution focalized to the center of main extended source but failed to reconstruct the focal source region. However, the reconstructed source by BMCE is much more accurate as reconstructing both focal and extended patterns of the source.

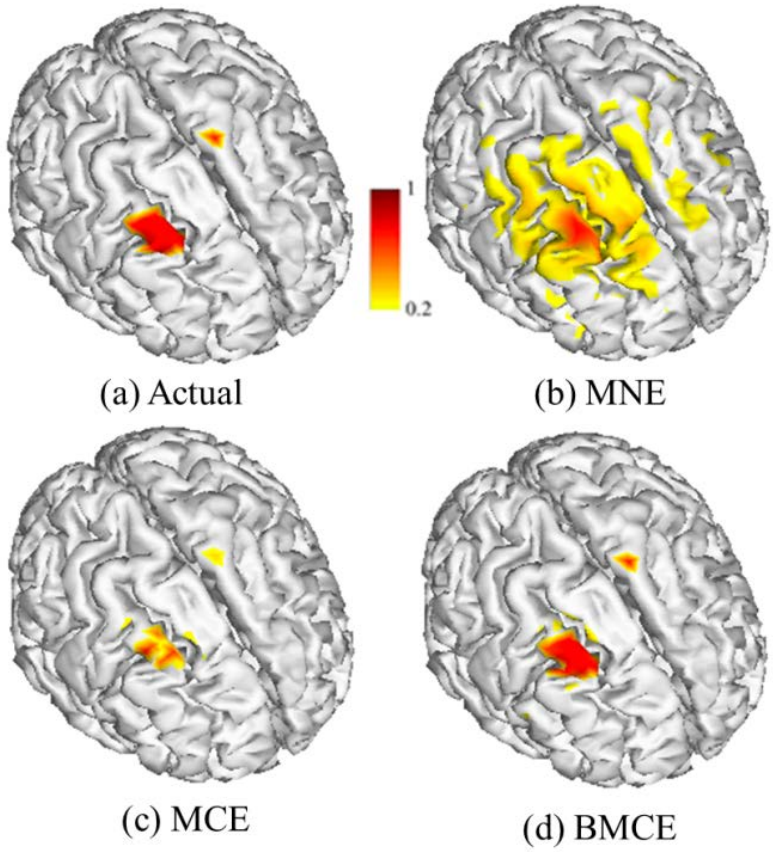

Figure 6.4. (a) Simulated actual sources and the corresponding reconstructed results using different methods, (b) MNE, (c) MCE and (d) BMCE

Figure 6.5, we simulated the case that two clusters have different amplitudes. MNE solution again distributed around and between of two sources. And MCE solution localized to the center of each sources but failed to recover the extension of two sources as focalized to the center of sources On the other hand, the reconstructed source by BMCE is much more accurate as reconstructing two extended patterns of the actual source.

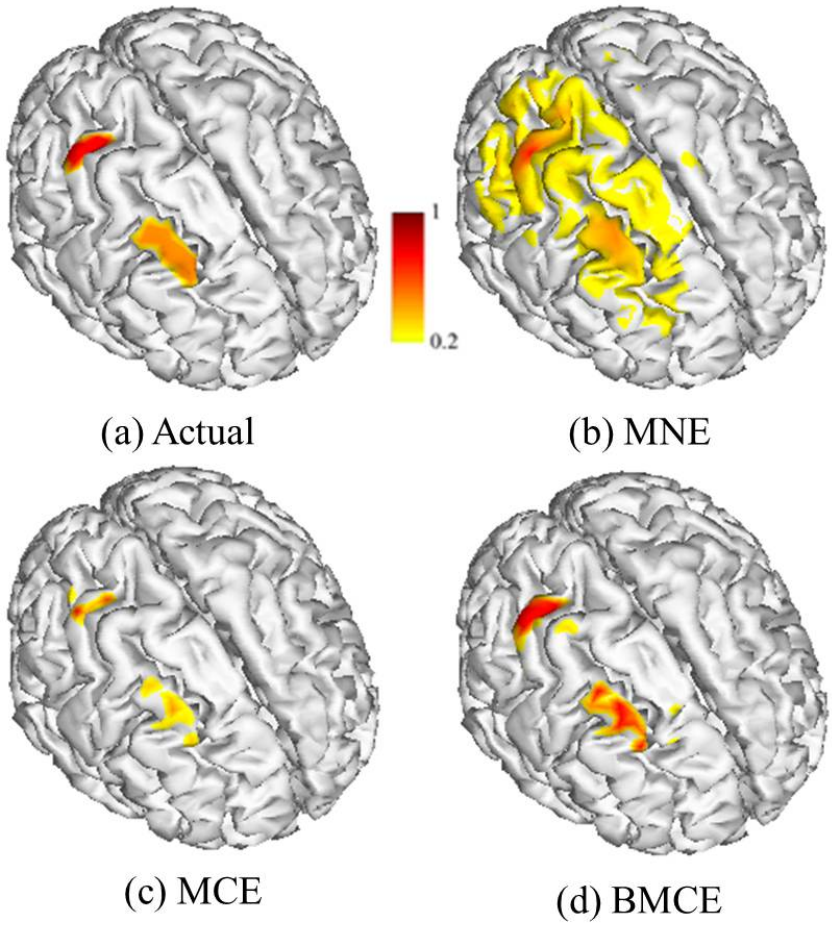

Figure 6.5. (a) Simulated actual sources and the corresponding reconstructed results using different methods, (b) MNE, (c) MCE and (d) BMCE

Table 6.3 summarizes the result of massive simulation with two clusters have different amplitudes. Two clusters are selected among the almost uniformly distributed 200 source locations on the cortical surface of right and left hemispheres. Therefore 100*100 samples are simulated and evaluated by quantitative measures. The amplitudes of source in each cluster are defined 10 and 20 and the area of activated source is averagely 11.3 and 69.6 mm^2 correspondingly. It could be readily observed from the table that MNE is accurate for the extended source and MCE is accurate for the focalized source. BMCE is much more accurate than two conventional methods regardless the extension of the source area. The intuitive and quantitative comparisons suggest that the proposed BMCE enhances the estimation accuracy.

Table 6.3. The result of massive simulation with two peaks

method	***RMSE***	***DF***	***CC***	***WCC***	***T (s)***
MNE	51.64	11.15	0.23	0.33	0.12
MCE	45.13	25.12	0.33	0.42	0.54
BMCE*	10.46	59.73	0.79	0.73	0.55
BMCE	12.82	55.72	0.72	0.69	5.51

6.3 Application to Localization of Epileptic Zone

The clinical uses of EEG and MEG are in detecting and localizing pathological activity in patients with epilepsy, and in localizing eloquent cortex for surgical planning in patients with brain tumors or intractable epilepsy. The goal of epilepsy surgery is to remove the epileptogenic tissue while sparing healthy brain areas [81-84]. Knowing the exact position of essential brain regions (such as the primary motor cortex and primary sensory cortex, visual cortex, and areas involved in speech production and comprehension) helps to avoid surgically induced neurological deficits. EEG and MEG source localization play a major role in the prognosis and surgical planning for patients with intractable partial epilepsy. Therefore, we also applied the proposed BMCE method to localize the epileptic activity in a patient with medically intractable epilepsy requiring a respective surgery. Since Accurate estimation of activated region is crucial in planning the surgery, BMCE is expected to be promising.

The MR images of the patient were acquired using a regular T1-weighted sequence for head image. The slice thickness was 1.5 mm with acquisition in the sagittal orientation with matrix size of 256 by 256. Using scanned MR images, BEM models and a cortical source space were extracted using Brainstorm. MEG signal were acquired by the whole-head MEG system (MEG center, SNU hospital), which consists of 306 channels arranged in triplets of two planar gradiometers (204 channels) and one magnetometer (102 channels). The sampling frequency was 600.615Hz, and the signal was filtered by a band-pass filter in the range of

0.1~200Hz. Series of interictal spikes were classified and the base line of signal is corrected shown in Figure 6.6.

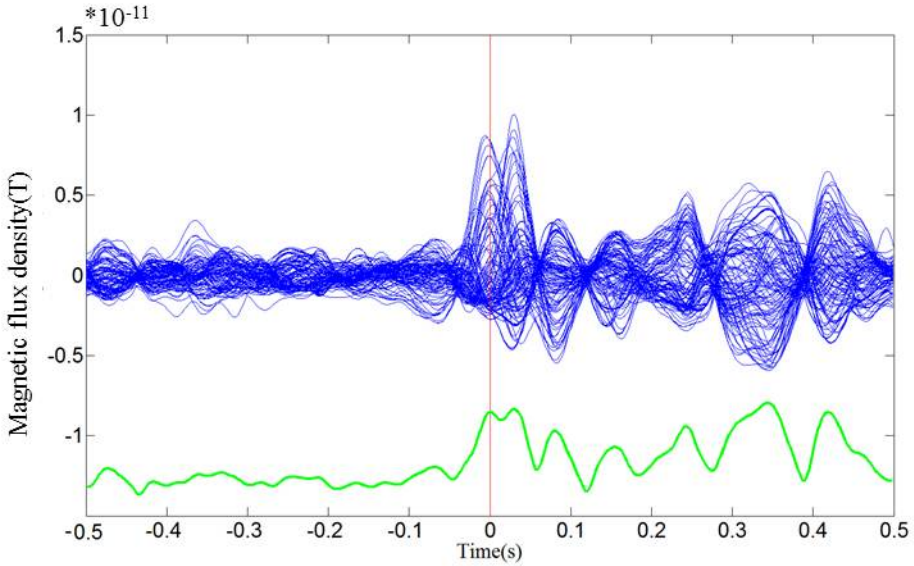

Figure 6.6. averaged interictal spike of MEG

Since the post-operative MR images of the patient (Figure 6.7) were also acquired, we thus know where the epileptogenic zone is, and therefore, the method can be verified against the exact location of epileptogenic zone. The resection area, the part of right temporal lobe, is marked with the cross lines in Figure 6.7 (a) sagittal, (b) transverse and (c) coronal view of the head. Note that the medical MR images are usually flipped horizontally.

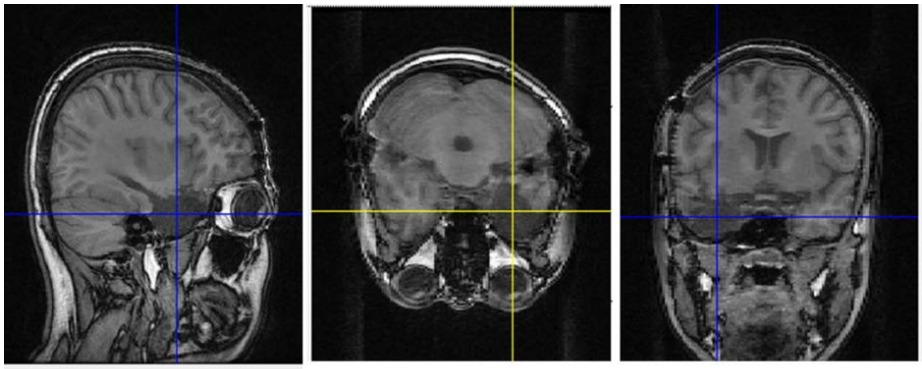

Figure 6.7. Post-surgery MR images of the patient. The cross lines in (a) sagittal, (b) transverse and (c) coronal views imply the center of the resection area.

As shown in Figure 6.8(a), we segmented the resection region from the post-operative MR images and co-registered the resection region to the segmented by pre-operative MR images using Brainstorm software.

For the head source modeling, the source space is consisted of 7,497 dipoles with 1.5mm distance between the nearest two dipoles. A piecewise homogeneous and isotropic approximation with constant conductivity, 0.3, 0.06, 0.3 S/m was adopted for boundary element method to calculate the forward magnetic field and electric potential distributions with 729, 843 and 986 points for skin, outer skull and inner skull respectively. The region of interest is also restricted to the part of cortical surface which is further than 5mm from the inner skull surface. The generation of cortical surface, boundary element meshes and leadfield matrix for MEG forward problems is computed with Brainstorm.

Figure 6.8 (b) shows that the reconstructed source obtained from MNE is overly distributed over whole cortical surface. MCE estimated source which is very concentrated to the center of the resection region. However, the BMCE seems to be more effective, it obtains more focused source distribution and the epileptic zone is well localized.

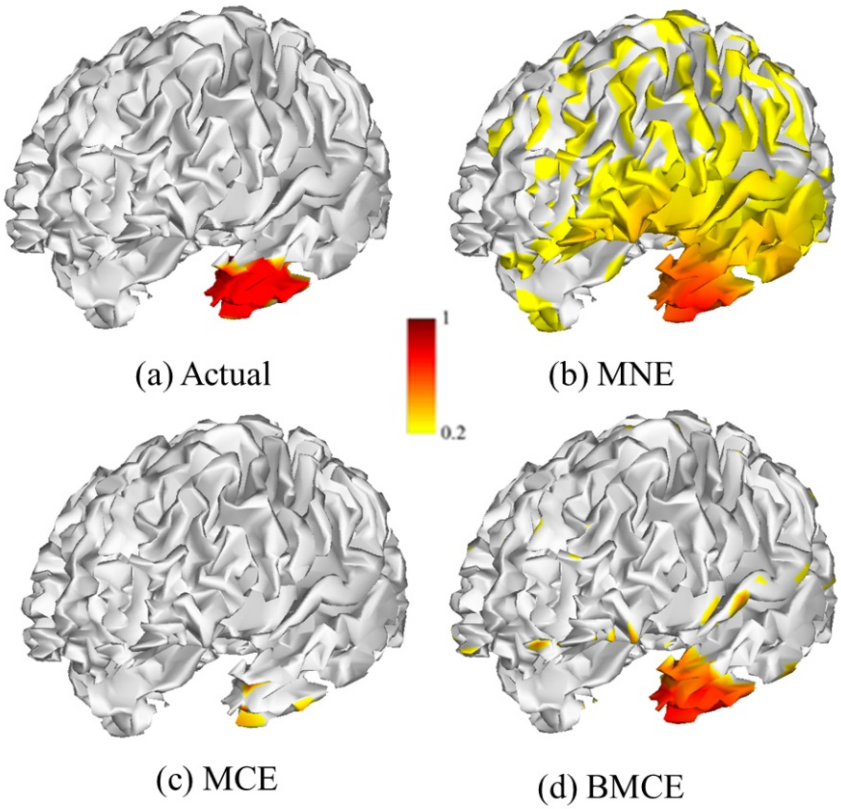

Figure 6.8. (a) The actual resection region co-registered on the cortical surface and reconstructed source by (b) MNE, (c) MCE and (d) BMCE

5. Conclusion

This dissertation focused on the localization of the neuroelectromagnetic source distributed on the human cortical surface and proposed two algorithms solving inverse problems of EEG/MEG data based on the directional characteristics of EEG/MEG source and the constraint of maximum current density.

First we proposed a new multimodal cortical source imaging method to integrate simultaneously recorded EEG and MEG recordings, which takes into account the directional sensitivities of the two modalities. The different sensitivities of EEG and MEG to source orientations have been investigated by several research groups. However, consideration of the directional sensitivity characteristics in the integrated EEG/MEG source imaging has not been reported prior to our study. Previous studies concerning integrated EEG and MEG source imaging have focused only on how to preprocess EEG and MEG leadfield matrices to reduce the condition number of the combined linear system. We developed an explicit formulation based on WMNE with a source weighting matrix reflecting the decomposed directional components of EEG and MEG, yielding results robust to the cortical source orientations. Our simulation studies showed that the proposed method can enhance the source localization accuracy significantly, regardless of the cortical source locations.

Second we proposed a new inverse algorithm for the improvement of source estimation regardless the extension of source distribution. The additional maximum amplitude constraint in MCE does successively enhance the localization accuracy in

EEG/MEG source imaging and the maximum bound of sources is also estimated through L-curve analysis of the L1 norm of sources with respect to the maximum bound. To overcome weakness of L1 minimization approach in regularization, we introduced an intrinsic regularization method without any additional parameters.

The proposed approaches are applied to various realistic computer simulation and practical experiment and evaluated by the quantitative analysis and comparison with conventional methods. For the accurate and reliable simulation closed to real problem, instead of simple sphere model, the complex geometry of head and conductivities obtained by a MR image and practical experiments respectively is employed to describe the current sources and induced the electromagnetic fields.

Under various conditions of source and situation, i.e., directional properties of sources, position and extension of sources, addition of sensor noise, multiple clusters of sources with different size or strength, we performed numerous simulation of source reconstruction with the conventional and proposed methods. Then to analyze the results quantitatively, we introduced several conventional evaluation methods and proposed a new method named weighted correlation coefficient (WCC) to verify the performance of proposed reconstruction algorithms. Moreover, we applied the proposed method to MEG practical measurement to estimate the epileptic zone in a patient with medically intractable epilepsy requiring a respective surgery. Since Accurate estimation of epileptic zone is crucial in planning the surgery, the proposed method is expected to be promising. As a result, compared to the reconstructed source obtained from conventional methods is overly distributed over whole cortical

surface or very concentrated to the center of the resection region, the proposed method successfully reconstructed the position and extension of the resection region.

In the future, more researches are expected to be continued. First, two proposed algorithms can be combined. When EEG and MEG data are recorded simultaneously, the additional constraint term of maximum bound of source amplitude also can be combined with the weight considering the directional characteristics of source. Second, the proposed algorithm can be extended to solve the spatio-temporal EEG/MEG estimation problem under the situation that noise level is varying. In addition, the computation time of BMCE can be reduced by estimating the maximum bound in one step process without pre-computation of the maximum bound.

References

[1] S.R. Cherry, and M.E. Phelps, “Imaging brain function with positron emission tomography,” in *Brain Mapping: The Methods*, Toga AW and Mazziotta JC Eds., Academic, New York, 1996.

[2] A.M. Howseman, and R.W. Bowtell, “Functional magnetic resonance imaging: Imaging techniques and contrast mechanisms,” Philos. Trans. R. Soc. London B, Biol. Sci., vol. 354, pp.1179-1194, 1999.

[3] A. Villringer, and B. Chance, “Noninvasive optical spectroscopy and imaging of human brain function,” Trends Neurosci., vol. 20, pp.435-442, 1997.

[4] M.S. Hämäläinen, R. Hari, R.J. Ilmoniemi, J. Knuutila, and O.V. Lounasmaa, “Magnetoencephalography. Theory, instrumentation and applications to the noninvasive study of human brain function,” Rev. Mod. Phys., vol. 65, pp.413-497, 1993.

[5] P.L. Nunez, “Electric fields of the brain,” Oxford Univ. Press, 1981.

[6] S. Knake, E. Halgren, H. Shiraishi, K. Hara, H.M. Hamer, P.E. Grant, V.A. Carr, D. Foxe, S. Camposano, and E. Busa, “The value of multichannel MEG and EEG in the presurgical evaluation of 70 epilepsy patients,” Epilepsy Research., vol. 69, pp.80-86, 2006.

[7] S. Baillet, J.C. Mosher, and R.M. Leahy, “Electromagnetic Brain Mapping,” IEEE Signal Process. Mag., Nov., pp.14-30, 2001.

[8] H. Yoshinaga, T. Nakahori, Y. Ohtsuka, E. Oka, Y. Kitamura, H. Kiriyama, K. Kinugasa, K. Miyamoto, and T. Hoshida, “Benefit of simultaneous recording of EEG and MEG in dipole localization,” Epilepsia., vol. 43, pp.924-928, 2002.

[9] C.C. Wood, “Application of dipole localization methods to source identification of human evoked potentials,” Ann. N. Acad. Sci., vol. 338, pp.139-155, 1982.

[10] A. Molins, S.M. Stufflebeam, E.N. Brown, and M.S. Hämäläinen, “Quantification of the benefit from integrating MEG and EEG data in minimum ℓ2-norm estimation,” Neuroimage., vol. 42, pp.1069-1077, 2008.

[11] T. Bast, G. Ramantani, T. Boppel, T. Metzke, O. Ozkan, C. Stippich, A. Seitz, A. Rupp, D. Rating, and M. Scherg, “Source analysis of interictal spikes in polymicrogyria: loss of relevant cortical fissures requires simultaneous EEG to avoid MEG misinterpretation,” Neuroimage., vol. 25, pp.1232-1241, 2005.

[12] R.M. Leahy, J.C. Mosher, M.E. Spencer, M.X. Huang, and J.D. Lewine, “A study of dipole localization accuracy for MEG and EEG using a human skull phantom,” Electroenceph. Clin. Neurophysiol., vol.107, pp.159-173, 1998.

[13] J.S. Ebersole, K. Squires, J. Gamelin, J. Lewine, and M. Scherg, “Simultaneous MEG and EEG provide Complementary dipole models of temporal lobe spikes,” Epilepsia., vol. 34(Suppl 6), pp.143, 1993.

[14] D.Y. Ko, C. Kufta, D. Scaffidi, and S. Sato, “Source localization determined by magnetoencephalography and electroencephalography in temporal lobe epilepsy: comparison with eletrocorticography: technical case report,” Neurosurgery., vol.42, pp.414-421, 1998.

[15] N. Nakasato, M.F. Levesque, D.S. Barth, C. Baumgartner, R.L. Rogers, and W.W. Sutherling, “Comparisons of MEG, EEG, and ECoG source localization in neocortical partial epilepsy in humans,” Electroenceph. Clin. Neurophysiol., vol.91, pp.171-178, 1994.

[16] C. Baumgartner, “Controversies in clinical neurophysiology. MEG is superior to EEG in the localization of interictal epileptiform activity: Con,” Clin. Neurophysiol., vol.115, pp.1010-1020, 2004.

[17] M.S. Hämäläinen, and R. J. Ilmoniemi, “Interpreting magnetic fields of the brain: Minimum norm estimates,” Med. & Bio. Eng. Comp., vol. 32, pp.35-42, 1994.

[18] K. Uutela, M. Hamalainen, and E. Somersalo, “Visualization of magnetoencephalographic data using minimum current estimates,” Neuroimage., vol.10, pp.173-180, 1999.

[19] R.D. Pascual-Marqui, C.M. Michel, and D. Lehmann, “Low resolution electromagnetic tomography: A new method for localizing electrical activity in the brain,” Int. J.

Psychophysiol., vol. 18, pp. 49–65, 1994.

[20] I.F. Gorodnitsky, J.S. George, and B.D. Rao, “Neuromagnetic source imaging with FOCUSS: A recursive weighted minimum norm algorithm,” Electroenceph. Clin. Neurophysiol., vol. 95, pp. 231–251, 1995.

[21] E. Niedermeyer, and F.L. Da Silva, Electroencephalography: Basic Principles, Clinical Applications, and Related Fields., Lippincot Williams & Wilkins, p. 1258, 1999.

[22] Walter WG, Walter VJ. “The electrical activity of the brain”. Annu Rev Physiol., vol. 11, pp. 199- 230, 1949.

[23] B. Abou-Khalil, K.E. Musilus, “Atlas of EEG & Seizure Semiology,” Elsevier, 2005.

[24] J.S. Ebersole, and S.V. Pacia, “Localization of temporal lobe foci by ictal EEG patterns,” Epilepsia., vol. 37, pp. 386–399, 1996.

[25] G. Gargiulo, P. Bifulco, R.A. Calvo, M. Cesarelli, C. Jin, and A. Van Schaik, “A mobile EEG system with dry electrodes,” Proc. IEEE Biomed Conf., pp. 273–276, 2008.

[26] C.T. Lin, L.W. Ko, J.C. Chiou, J.R. Duann, T.W. Chiu, R.S. Huang, S.F. Liang, and T.P. Jung, “Noninvasive neural prostheses using mobile and wireless EGG,” Proc. IEEE., vol. 97, pp. 1167–1183, 2008.

[27] S. Baillet, L. Garnero, G. Marin, and J.P. Hugonin, “Combined MEG and EEG source imaging by minimization of mutual information,” IEEE Trans. Biomed. Eng., vol. 46, pp. 522–534, 1999.

[28] E.R. Kendal, J.H. Schwartz, and T.M. Jessell, “Principles of Neural Science”, 4th Ed., McGraw-Hill, 2000.

[29] R. Cooper, A.L. Winter, H.J. Crow, W.W. Grey, “Comparison of subcortical, cortical and scalp activity using chronically indwelling electrodes in man,” Electroenceph. Clin. Neurophysiol., vol. 18, pp. 217-228, 1965.

[30] J.S. Ebersole, “Noninvasive localization of epileptogenic foci by EEG source modeling,” Epilepsia, vol. 41, pp.24–33, 2000.

[31] J.X. Tao, A. Ray, S. Hawes-Ebersole, J.S. Ebersole, “Intracranial EEG substrates of scalp EEG interictal spikes,” Epilepsia, vol. 46, pp.669-676, 2005.

[32] M. Oishi, H. Otsubo, S. Kameyama, N. Morota, H. Masuda, M. Kitayama, R. Tanaka, “Epileptic spikes: magnetoencephalography versus simultaneous electrocorticography,” Epilepsia, vol. 43, pp.1390-1395, 2002.

[33] N. Mikuni, T. Nagamine, A. Ikeda, K. Terada, W. Taki, J. Kimura, H. Kikuchi, H. Shibasaki, “Simultaneous recording of epileptiform discharges by MEG and subdural electrodes in temporal lobe epilepsy,” Neuroimage, vol. 5, pp.298-306, 1997.

[34] S.R. Jones, D.L. Pritchett, M.A. Sikora, S.M. Stufflebeam, M. Hämäläinen, C.L. Moore, “Quantitative analysis and biophysically realistic neural modeling of the MEG murhythm: rhythmogenesis and modulation of sensory-evoked responses,” J.Neurophysiol, vol. 102, pp.3554-3572, 2009.

[35] A.F. Cheung, A.A Pollen, A. Tavare, J. DeProto, Z. Molnar, “Comparative aspects of cortical neurogenesis in vertebrates,” J. Anat., vol. 211, pp.164–176, 2007.

[36] J. Sarvas, “Basic mathematical and electromagnetic concepts of the Biomagnetic inverse problem,” Phys. Med. Biol., vol. 32, pp.11-22, 1987.

[37] R.V. Uitert and C. Johnson, “Can a Spherical Model Substitute for a Realistic Head Model in Forward and Inverse MEG Simulations?,” Proc. Conf. Biomagnetism 2002, Jena, Germany, 2002.

[38] D. Yao, “Electric potential produced by a dipole in a homogeneous conducting sphere,” IEEE Trans. Biomed. Eng., vol. 47, pp.964-966, 2000.

[39] C.H. Im and B. He, “On the Accurate Anatomical Constraints in EEG/MEG Source Imaging,” International Journal of Bioelectromagnetics, vol. 8, no. 1, pp. III/1-III/11, 2006.

[40] H. Buchner, G. Knoll, M. Fuchs, A. Rienäcker, R. Beckmann, M. Wagner, J. Silny, and P. Jorg, “Inverse localization of electric dipole current sources in finite element models of the human head,” Electroenceph. Clin. Neurophysiol., vol.102, pp.267-278, 1997.

[41] S. Baillet, J. Riera, L. Garnero, G. Marin, J. Mangin, and J. Aubert, “Evaluation of inverse methods and head models for EEG source localization using a human skull phantom,” Phys. Med. Biol, vol. 46, no. 1, pp.77–96, 2001.

[42] D.S. Tuch, V.J. Wedeen, A.M. Dale, J.S. George, and J.W. Belliveau, “Conductivity

mapping of biological tissue using diffusion MRI," Ann. N. Acad. Sci., vol. 888, pp.314-316, 1999.

[43] S. Abboud, M. Rosenfeld, and J. Luzon, "Effect of source location on the scalp potential asymmetry in a numerical model of the head," IEEE Trans. Magn. vol. 43, no. 7, pp.690-696, 1996.

[44] Y.Q. Xie, J.S. Yuan, X.S. Ma, and X. Guan, "Calculation of EEG problems with anisotropic conducting media by the finite volume method," IEEE Trans. Magn., vol. 37, no. 5, pp. 3749-3752, 2001.

[45] A.M. Dale and M.I. Sereno, "Improved localization of cortical activity by combining EEG and MEG with MRI surface reconstruction: a linear approach," J. Cognit. Neurosci., vol. 5, pp.162-176, 1993.

[46] M.S. Hämäläinen and R.J. Ilmoniemi, "Interpreting measured magnetic fields of the brain: Estimates of current distributions," Technical Report TKK-F-A559, Helsinki University of Technology, 1984.

[47] K. Matsuura and U. Okabe, "Selectiveminimum-norm solution of the biomagnetic inverse problem," IEEE Trans. Biomed. Eng. 42: 608–615, 1995

[48] J.P. Evans and R.E. Steuer, A revised simplex method for linear multiple objective programs, Mathematical Programming, 1973

[49] S. Mehrotra, "On the Implementation of a Primal-Dual Interior Point Method,". SIAM Journal on Optimization 2 (4): 575, 1992

[50] M.S. Hämäläinen, and J. Sarvas, "Realistic conductivity geometry model of the human head for interpretation of neuromagnetic data," IEEE Trans. on Biomedical Engineering, vol. 36, pp.165-171, 1989.

[51] C.H. Im, K.O. An, H.K. Jung, H. Kwon, and Y.H. Lee, "Assessment criteria for MEG/EEG cortical patch tests," Phys. Med. Biol, vol. 48, pp.2561-2573, 2003.

[52] S. Baillet, J. Riera, L. Garnero, G. Marin, J. Mangin, and J. Aubert, "Evaluation of inverse methods and head models for EEG source localization using a human skull phantom," Phys. Med. Biol, vol. 46, no. 1, pp.77–96, 2001.

[53] J.H. Choi, M.H. Kim, L. Feng, C.H. Lee and H.K. Jung, "A New Weighted Correlation

Coefficient Method to Evaluate Reconstructed Brain Electrical Sources," Journal of Applied Mathematics, 2012.

[54] A. Bartesaghi and G. Sapiro, "A system for the generation of curves on 3D brain images," Human Brain Mapping, vol. 14, pp.1–15, 2001.

[55] M.X. Huang, T. Song, D.J. Hagler, I. Podgorny, V. Jousmaki, L. Cui, K. Gaa, D.L. Harrington, A.M. Dale, and R.R. Lee, "A novel integrated MEG and EEG analysis method for dipolar sources," Neuroimage, vol. 37, pp.731-748, 2007.

[56] W.E. Kincses, C. Braun, S. Kaiser, and T. Elbert, "Modeling extended sources of event-related potentials using anatomical and physiological constraints," Human Brain Mapping, vol. 8, pp.182-193, 1999.

[57] J.S. Ebersole, K. Squires, J. Gamelin, J. Lewine, and Scherg, M., "Simultaneous MEG and EEG provide complementary dipole models of temporal lobe spikes," Epilepsia, 34(Suppl 6), 143. 1993

[58] H.M. Huizenga, T.L. Van Zuijen, D.J. Heslenfeld, and P.C.M. Molenaar, "Simultaneous MEG and EEG source analysis," Physics in Medicine and Biology, 46, pp.1737-1751, 2001

[59] H. Yoshinaga, T. Nakahori, Y. Ohtsuka, E. Oka, Y. Kitamura, H. Kiriyama, K. Kinugasa, K. Miyamoto, and T. Hoshida, "Benefit of simultaneous recording of EEG and MEG in dipole localization," Epilepsia, 43, pp.924-928, 2002

[60] D. Cohen and B.N. Cuffin, "Demonstration of useful differences between magnetoencephalogram and electroencephalogram," Electroencephalo-graphy and Clinical Neurophysiology, 56, pp.38-51, 1983

[61] D. Cohen and B.N. Cuffin, "Method for combining MEG and EEG to determine the sources," Physics in Medicine and Biology, 32, pp.85-89, 1987

[62] J.W. Phillips, R.M. Leahy, J.C. Mosher and B. Timsari, "Imaging neural activity using MEG and EEG," IEEE Engineering in medicine and biology magazine, 16, pp.34-42, 1997

[63] F. Babiloni, F. Carducci, F. Cincotti, C. Del Gratta, V. Pizzella, G.L. Romani, P.M. Rossini, F. Tecchio, and C. Babiloni, "Linear inverse source estimate of combined EEG

and MEG data related to voluntary movements", Human Brain Mapping, 14, pp.197-209, 2001

[64] M. Fuchs, M. Wagner, H.A. Wischmann, T. Kohler, A. Theißen, R. Drenckhahn and H. Buchner, "Improving source reconstructions by combining bioelectric and biomagnetic data," Electroencephalography and Clinical Neurophysiology, 107, pp.93-111, 1998

[65] R.N. Henson, E. Mouchlianitis, and K.J. Friston, "MEG and EEG data fusion: Simultaneous localisation of face-evoked responses," Neuroimage, 47, pp.581-589, 2009

[66] G.H. Golub, M. Heath, and G. Wahba, "Generalized cross-validation as a method for choosing a good ridge parameter," Technometrics, vol. 21, pp.215-223, 1979.

[67] J.H. Choi, Y.J. Jung, H.K. Jung, and C.H. Im. "A new multimodal cortical source imaging algorithm for integrating simultaneously recorded EEG and MEG." Inverse Problems in Science and Engineering, in press, 2012.

[68] G. Murty, Katta, Linear programming. New York: John Wiley & Sons, 1983

[69] G. B. Dantzig, "Linear Programming and Extensions," Princeton University Press, Prince-ton, NJ, 1963.

[70] A. Schrijver, "Theory of Linear and Integer Programming,". John Wiley & sons, 1998

[71] Maros, István; Mitra, Gautam, "Simplex algorithms". In J. E. Beasley. Advances in linear and integer programming. Oxford Science, 1996

[72] S. J. Wright, "Stability of linear equations solvers in interior-point methods," SIAM J. Mat. Anal. Appls., 16, pp. 1287-1307, 1995

[73] R. Fourer and S. Mehrotra, "Solving symmetric indefinite systems in an interior-point method for linear programming," Math. Prog. 62(1), 1993

[74] J. J. H. Forrest and J. A. Tomlin, "Implementing interior point linear programming methods in the Optimization Subroutine Library," IBM Systems J., 31(1), 1992.

[75] M.S. Bazaraa, J.J. Jarvis, H.D. Sherali, M.S. Bazaraa, "Linear programming and network flows," Wiley Online Library, 1990

[76] R.H. Bartels, G.H. Golub, "The simplex method of linear programming using LU

decomposition," Communications of the ACM, 1969

[77] M. Berkelaar, K. Eikland, and P. Notebaert, lpSolve: Open Source (Mixed-Integer) Linear Programming System. GNU LGPL (Lesser General Public License). 2004

[78] P. Hansen, "The L-curve and its use in the numerical treatment of inverse problems," IMM, Department of Mathematical Modelling, Technical Universityof Denmark, 1999.

[79] P. Hansen, "Analysis of discrete ill-posed problems by means of the L-curve," SIAM Rev., vol. 34, pp.561-580, 1992.

[80] M Hanke, "Limitations of the L-curve method in ill-posed problems, BIT Numerical Mathematics," Springer, 1996

[81] H.O. Luders, "Epilepsy surgery," New York Raven Press, 1992.

[82] G. Lantz, C.M. Michel, R.D. Pascual-Marqui, L. Spinelli, M. Seeck, S. Seri, T. Landis, and I. Rosen, "Extracranial localization of intracranial interictal epileptiform activity using LORETA (low resolution electromagnetic tomography)," Electroencephalogr. Clin. Neurophysiol., vol. 102, pp.414-422, 1997.

[83] Y.Y. Lin, K.P. Chang, J.C. Hsieh, T.C. Yeh, H.Y. Yu, S.Y. Kwan, D.J. Yen, C.H. Yiu, and R. Hari, "Magnetoencephalographic analysis of bilaterally synchronous discharges in benign Rolandic epilepsy of childhood," Seizure, vol. 12, pp.448-455, 2003.

[84] J.S. Ebersole, "Noninvasive localization of the epileptogenic focus by EEG dipole modeling," Acta Neurol. Scand., vol. 152(Suppl.), pp.20-28, 1994.

Appendix A. Derivation of L2 Norm Minimization Problem

The L2 linear inverse operator that used in this dissertation can be derived in various ways. All derivations arrive at equivalent inverse operators, when certain initial conditions are given.

The minimization of expected error begins with a set of measurements

$$\mathbf{x} = \mathbf{A}\mathbf{s} + \mathbf{n} \tag{A.1}$$

where **x** is the measurement vector, **A** is the gain matrix, **s** is the strength of each dipole component, and **n** is the noise vector. One would like to calculate a linear inverse operator **W** that minimizes the expected difference between the estimated and the correct source solution. The expected error can be defined as:

$$\mathbf{Err}_{\mathbf{W}} = <\| \mathbf{W}\mathbf{x} - \mathbf{s} \|^2>. \tag{A.2}$$

Here we assume that both **n** and **s** are normally distributed with zero mean. Using their corresponding covariance matrices **C** and **R**, the expected error can be rewritten as:

$$\mathbf{Err}_{\mathbf{W}} = <\| \mathbf{W}(\mathbf{A}\mathbf{s} + \mathbf{n}) - \mathbf{s} \|^2> \tag{A.3}$$

$$= <\| (\mathbf{W}\mathbf{A} - \mathbf{I})\mathbf{s} + \mathbf{W}\mathbf{n}) \|^2> \tag{A.4}$$

$$= <\| (\mathbf{M}\mathbf{s} + \mathbf{W}\mathbf{n}) \|^2> \tag{A.5}$$

where $\mathbf{M} = \mathbf{W}\mathbf{A} - \mathbf{I}$

$$= \langle \| \mathbf{Ms} \|^2 \rangle + \langle \| \mathbf{Wn} \|^2 \rangle \tag{A.6}$$

$$= \mathrm{tr}(\mathbf{MRM}^T) + \mathrm{tr}(\mathbf{WCW}^T) \tag{A.7}$$

where tr(**A**) is the trace of **A** and is defined as the sum of the diagonal entries. Re-expanding the expression gives:

$$= \mathrm{tr}(\mathbf{WARA}^T\mathbf{W}^T - \mathbf{RA}^T\mathbf{W}^T - \mathbf{WAR} + \mathbf{R}) + \mathrm{tr}(\mathbf{WCW}^T). \tag{A.8}$$

This expression can be explicitly minimized by taking the derivative with respect to **W**, setting it to zero and solving for **W**.

$$0 = 2\mathbf{WARA}^T - 2\mathbf{RA}^T + 2\mathbf{WC} \tag{A.9}$$

Solving for **W**:

$$\mathbf{WARA}^T + \mathbf{WC} = \mathbf{RA}^T \tag{A.10}$$

$$\mathbf{W}(\mathbf{ARA}^T + \mathbf{C}) = \mathbf{RA}^T. \tag{A.11}$$

This yields the expression for the linear inverse operator:

$$\mathbf{W} = \mathbf{RA}^T(\mathbf{ARA}^T + \mathbf{C})^{-1}. \tag{A.12}$$

The Bayesian linear inverse derivation begins with the expression for conditional probability:

$$\mathrm{P}(\mathbf{s} \mid \mathbf{x}) = \frac{\mathrm{P}(\mathbf{x} \mid \mathbf{s})\mathrm{P}(\mathbf{s})}{\mathrm{P}(\mathbf{x})} \tag{A.13}$$

which one would like to maximize. Beginning with a measurement vector **x**:

$$\mathbf{x} = \mathbf{As} + \mathbf{n} \tag{A.14}$$

where **A** is the gain matrix, **s** is the strength of each dipole component, and **n** is the noise vector. Assuming both **n** and **s** are normally distributed with zero mean and covariance matrices **C** and **R**, respectively, one can rewrite P(**x**|**s**) and P(**s**):

$$P(\mathbf{x}\,|\,\mathbf{s})\alpha e^{-(\mathbf{As}-\mathbf{x})^T\mathbf{C}^{-1}(\mathbf{As}-\mathbf{x})} \tag{A.15}$$

$$P(\mathbf{s})\alpha e^{-\mathbf{s}^T\mathbf{R}^{-1}\mathbf{s}}. \tag{A.16}$$

This gives a simplified Bayesian expression:

$$\max[P(\mathbf{s}\,|\,\mathbf{x})] = \max\left[\frac{(e^{-(\mathbf{As}-\mathbf{x})^T\mathbf{C}^{-1}(\mathbf{As}-\mathbf{x})})(e^{-\mathbf{s}^T\mathbf{R}^{-1}\mathbf{s}})}{P(\mathbf{x})}\right] \tag{A.17}$$

$$= \max[-(\mathbf{As}-\mathbf{x})^T\mathbf{C}^{-1}(\mathbf{As}-\mathbf{x})-\mathbf{s}^T\mathbf{R}^{-1}\mathbf{s}] \tag{A.18}$$

$$= \min[(\mathbf{As}-\mathbf{x})^T\mathbf{C}^{-1}(\mathbf{As}-\mathbf{x})+\mathbf{s}^T\mathbf{R}^{-1}\mathbf{s}] \tag{A.19}$$

$$= \min[\mathbf{s}^T\mathbf{A}^T\mathbf{C}^{-1}\mathbf{As}-\mathbf{s}^T\mathbf{A}^T\mathbf{C}^{-1}\mathbf{x}-\mathbf{x}^T\mathbf{C}^{-1}\mathbf{As}+\mathbf{x}^T\mathbf{C}^{-1}\mathbf{x}+\mathbf{s}^T\mathbf{R}^{-1}\mathbf{s}]. \tag{A.20}$$

Taking the derivative with respect to **s** and setting it to zero:

$$2\mathbf{A}^T\mathbf{C}^{-1}\mathbf{As}-2\mathbf{A}^T\mathbf{C}^{-1}\mathbf{x}+2\mathbf{R}^{-1}\mathbf{s}=0. \tag{A.21}$$

Solving for **s** gives:

$$\mathbf{s}=(\mathbf{A}^T\mathbf{C}^{-1}\mathbf{A}+\mathbf{R}^{-1})^{-1}\mathbf{A}^T\mathbf{C}^{-1}\mathbf{x}=\mathbf{Wx} \tag{A.22}$$

which yields the expression for the Bayesian linear operator

$$\mathbf{W}=(\mathbf{A}^T\mathbf{C}^{-1}\mathbf{A}+\mathbf{R}^{-1})^{-1}\mathbf{A}^T\mathbf{C}^{-1}. \tag{A.23}$$

The above Bayesian linear operator is very similar to that derived using Tikhonov regularization. Again, one begins with a measurement vector **x**:

$$\mathbf{As} = \mathbf{x}\,. \tag{A.24}$$

A smoothing functional **F** is defined as:

$$\mathbf{F} = \| \mathbf{As} - \mathbf{x} \|^2 + \lambda \| \mathbf{Ms} \|^2 \tag{A.25}$$

where λ and **M** are added for regularization. To calculate the operator, the smoothing functional is explicitly minimized (taking its derivative and setting it to zero). Solving for **s**:

$$0 = 2\mathbf{A}^T\mathbf{As} - 2\mathbf{A}^T\mathbf{x} + 2\lambda\mathbf{M}^T\mathbf{Ms} \tag{A.26}$$

$$(\mathbf{A}^T\mathbf{A} + \lambda\mathbf{M}^T\mathbf{M})\mathbf{s} = \mathbf{A}^T\mathbf{x} \tag{A.27}$$

$$\mathbf{s} = (\mathbf{A}^T\mathbf{A} + \lambda\mathbf{M}^T\mathbf{M})^{-1}\mathbf{A}^T\mathbf{x} = \mathbf{Wx} \tag{A.28}$$

$$\mathbf{W} = (\mathbf{A}^T\mathbf{A} + \lambda\mathbf{M}^T\mathbf{M})^{-1}\mathbf{A}^T\,. \tag{A.29}$$

This is equivalent to the Bayesian linear operator when $\mathbf{C} = \mathbf{C}^{-1} = \mathbf{I}$ and $\lambda\mathbf{M}^T\mathbf{M} = \mathbf{R}^{-1}$. Wiener filtering (also known as the Kalman-Bucy method) filtering uses an optimal linear filter to minimize the expected error between the actual source (i.e., input) and the estimated source (i.e., noisy output):

$$\mathbf{Err}_\mathbf{W} = <\| \mathbf{Wx} - \mathbf{s} \|^2>\,. \tag{A.30}$$

The operator must satisfy the Wiener-Hopf equation:

$$\mathbf{\Psi}_{\mathbf{sx}} = \mathbf{W}\mathbf{\Psi}_\mathbf{x} \tag{A.31}$$

where $\mathbf{\Psi}_{\mathbf{sx}} = <\mathbf{sx}^T>$ and $\mathbf{\Psi}_\mathbf{x} = <\mathbf{xx}^T>$. Expanding the covariance terms gives:

$$<\mathbf{s}[\mathbf{As} + \mathbf{n}]^T> = \mathbf{W} <[\mathbf{As} + \mathbf{n}][\mathbf{As} + \mathbf{n}]^T> \tag{A.32}$$

$$< \mathbf{s}\mathbf{s}^T\mathbf{A}^T + \mathbf{s}\mathbf{n}^T > = \mathbf{W} < \mathbf{A}\mathbf{s}\mathbf{s}^T\mathbf{A}^T + \mathbf{n}\mathbf{s}^T\mathbf{A}^T + \mathbf{A}\mathbf{s}\mathbf{n} + \mathbf{n}\mathbf{n}^T > . \quad \text{(A.33)}$$

Because the signal and noise are independent, the signal-noise covariance terms (e.g., $<\mathbf{s}\mathbf{n}^T>$) equal zero, leaving:

$$< \mathbf{s}\mathbf{s}^T\mathbf{A}^T > = \mathbf{W} < \mathbf{A}\mathbf{s}\mathbf{s}^T\mathbf{A}^T + \mathbf{n}\mathbf{n}^T > . \quad \text{(A.34)}$$

Again, because the signal and noise are independent, we can separate the terms on the right side:

$$< \mathbf{s}\mathbf{s}^T\mathbf{A}^T > = \mathbf{W}(< \mathbf{A}\mathbf{s}\mathbf{s}^T\mathbf{A}^T > + < \mathbf{n}\mathbf{n}^T >) \quad \text{(A.35)}$$

$$\mathbf{R}\mathbf{A}^T = \mathbf{W}(\mathbf{A}\mathbf{R}\mathbf{A}^T + \mathbf{C}). \quad \text{(A.36)}$$

Thus, the inverse operator is:

$$\mathbf{W} = \mathbf{R}\mathbf{A}^T(\mathbf{A}\mathbf{R}\mathbf{A}^T + \mathbf{C})^{-1} \quad \text{(A.37)}$$

Appendix B. Derivation of Directional Inverse Operators

The directional inverse operator, $G_{t,eeg}$, can be computed as follows. Applying (5) and (11), the estimated source can be written as

$$\hat{\mathbf{j}} = P_t^{-1} G_{t,meg} \mathbf{b_t}. \tag{B.1}$$

Using (9), (A.1) can be rewritten as

$$\hat{\mathbf{j}} = P_t^{-1} G_{t,meg} K_{t,meg} \mathbf{j_t}, \tag{B.2}$$

and from (5)

$$\hat{\mathbf{j}} = P_t^{-1} G_{t,meg} K_{t,meg} P_t \mathbf{j}. \tag{B.3}$$

When we define the error between the exact and reconstructed sources $\boldsymbol{\varepsilon}$ as

$$\varepsilon = \mathrm{j} - \hat{\mathrm{j}}. \tag{B.4}$$

We can rewrite (A.3) as

$$\mathbf{j} = P_t^{-1} G_{t,meg} K_{t,meg} P_t \mathbf{j} + \boldsymbol{\varepsilon}. \tag{B.5}$$

Rearranging (A.5), we have the following relationship:

$$\boldsymbol{\varepsilon} = \left\{ I - P_t^{-1} G_{t,meg} K_{t,meg} P_t \right\} \mathbf{j}. \tag{B.6}$$

To find $G_{t,meg}$ that minimizes the error $\boldsymbol{\varepsilon}$ for any $\mathbf{j}$, we consider the following minimization problem:

$$\min_{G_{t,meg}} tr \left\{ \left(I - P_t^{-1} G_{t,meg} K_{t,meg} P_t \right) \left(I - P_t^{-1} G_{t,meg} K_{t,meg} P_t \right)^T \right\}, \tag{B.7}$$

where $tr\{\cdot\}$ is the trace of a matrix and is defined as the sum of the main diagonal entries. This expression can be explicitly minimized by taking the derivative with

respect to $G_{t,meg}$ using the following properties:

$$\begin{aligned}\frac{\partial tr(AXB)}{\partial X} &= BA,\\ \frac{\partial tr(AXBX^T C)}{\partial X} &= BX^T CA + B^T X^T A^T C^T\end{aligned} \tag{B.8}$$

and the derivative set to zero. Then, we have

$$G_{t,meg} = P_t^2 K_{t,meg}^T (K_{t,meg} P_t^2 K_{t,meg}^T)^{-1}. \tag{B.9}$$

The explicit formulations for $G_{t,eeg}$, $G_{r,eeg}$, and $G_{r,meg}$ can be derived in a similar way. Then, we have

$$\begin{aligned}G_{t,eeg} &= P_t^2 K_{t,eeg}^T (K_{t,eeg} P_t^2 K_{t,eeg}^T)^{-1},\\ G_{r,eeg} &= P_r^2 K_{r,eeg}^T (K_{r,eeg} P_r^2 K_{r,eeg}^T)^{-1},\\ G_{r,meg} &= P_r^2 K_{r,meg}^T (K_{r,meg} P_r^2 K_{r,meg}^T)^{-1}.\end{aligned} \tag{B.10}$$

Appendix C. Derivation of L1 Norm Minimization Problem

This appendix presents the way to solve the bounded and weighted L1 norm minimization problem with sensor noise. The problem is

$$\min_{\mathbf{j}} \left\| \mathbf{c}^{\mathrm{T}} \mathbf{j} \right\|_1 , \text{ subject to } \mathbf{b} = K\,\mathbf{j} + \mathbf{e} \;\; \& \;\; |j_i| \le p , \tag{C.1}$$

where **c** is a weighting vector and **e** is the sensor noise.

Since one of general form in linear programming (LP) is

$$\min_{\mathbf{j}} (\mathbf{c}^{\mathrm{T}} \mathbf{j}), \text{ subject to } \mathbf{b} = K\,\mathbf{j} \;\; \& \;\; j_{\mathrm{i}} \ge 0 , \tag{C.2}$$

(C.1) is required to be converted to the form of (C.2).

1) Regularization

Conventional regularization approach in L1-norm minimization problem is singular value decomposition of leadfield matrix. Let the leadfield matrix, K decomposed as following:

$$K = USV^T . \tag{C.3}$$

The minimum L1-norm solution is seeking the source distribution **j** that satisfies

$$U_{ng}\mathbf{b} = S_{ng}V_{ng}^T\mathbf{j} , \tag{C.4}$$

where S_{ng}, U_{ng} and V_{ng} contain the *ng* largest singular values and the associated singular vector, respectively. The optimal value for the regularization parameter *ng* depends on the signal-to-noise ratio of the measurements. The smaller *ng* is, the

greater the allowed mismatch between **b** and *K***j** can be while still satisfying constraint (C.4). The cutoff index *ng* is also the number of constraints in the LP problem; thus the maximum number of source locations having nonzero current is *ng*. This cutoff index has been determined by the user depending on the noise level without any guideline. In the paper which proposed MCE, the cutoff index is 30 when the noise is 10 % of the variance of the simulated data.

We introduce an intrinsic regularization method without any additional parameters. When the noise added on the measurements:

$$\mathbf{b} = K\,\mathbf{j} + \mathbf{e}, \tag{C.4}$$

though almost randomly generated noise is impossible to separate but in many physical experiments the noise is bounded by certain level. If we only estimate or experientially assume the maximum bound of noise level then the equation can be written in

$$\mathbf{b} - K\,\mathbf{j} < \max(\mathbf{e})\mathbf{i}\,, \tag{C.4}$$

where **i** is the vector whose element is 1.

This approach is much more intrinsic than the norm of noise or regularization parameter and easy to deal with the sensor noise. When the noise bounded by e* is added to the measurement then (C.1) yields

$$\min_{\mathbf{j}} \left\| \mathbf{c}^{\mathrm{T}}\mathbf{j} \right\|_1, \ \text{subject to } \left| \mathbf{b} - K\,\mathbf{j} \right| < \mathbf{e}^* \ \ \& \ \ \left| j_i \right| \le p\,, \tag{C.5}$$

which can be converted to the general form of linear programming.

2) L1 norm constraint

Because the current density can be either positive or negative, an additional step is needed to deal with the absolute values. It has been proposed to introduce two new non-negative variables; one can rewrite the L1 norm constraint term as

$$\min_{\mathbf{j}} \left\| \mathbf{c}^{\mathrm{T}} \mathbf{j} \right\|_1 = \min_{\mathbf{j}^+, \mathbf{j}^-} \mathbf{c}^{\mathrm{T}} \left(\mathbf{j}^+ + \mathbf{j}^- \right), \tag{C.5}$$

where

$$\mathbf{j} = \mathbf{j}^+ - \mathbf{j}^-, \tag{C.4}$$

and

$$0 \le j^+_i \le p, \; 0 \le j^-_i \le p \, . \tag{C.6}$$

3) The maximum bounded condition

The maximum bounded condition is also required to introduce two new non-negative variables. We can rewrite the bound condition

$$\left| j_i \right| \le p, \tag{C.5}$$

to

$$\begin{aligned} \mathbf{j}_i^+ - \mathbf{x}^+ &= p\mathbf{i}, \quad x_i^+ > 0 \\ \mathbf{j}_i^- - \mathbf{x}^- &= p\mathbf{i}, \quad x_i^- > 0. \end{aligned} \tag{C.7}$$

국문초록

뇌전도 및 뇌자도를 이용한 신경전자기 신호원 영상법은 분포전류원 모델의 경우, 추가적인 정보와 제한조건이 주어져야만 유일한 신호원을 복원할 수 있는 역문제이다.

본 학위 논문에서는 뇌전도 및 뇌자도를 이용한 신호원 영상법의 정확도를 향상시키기 위한 새로운 방법을 제안한다.

뇌자도는 대뇌피질상에 존재하는 반지름 방향의 신호원에 둔감한 반면 뇌전도는 뇌자도에 비해 상대적으로 방향성에 큰 영향을 받지 않는 것으로 알려져 있다. 이러한 신호원 고유의 방향 특성은 현재까지 분포전류원 모델의 신호원 추정에 적용되지 않았다. 본 학위 논문에서는 뇌전도와 뇌자도를 동시 측정한 경우에 대해 신호원의 방향성을 고려해 대뇌피질 상에 존재하는 신호원을 복원하는 방법을 제안하였다.

기존의 뇌전도/뇌자도 신호원 영상법을 통해 복원된 신호원은 실제 신호원과 비교했을 때 한점에 집중되거나 넓은 영역에 퍼져 있다. 따라서 다양한 분포 형태를 가진 신호원의 경우 기존 복원법을 통해서는 신호원의 분포 형태를 추정하기 힘들다는 단점이 있었다. 본 학위 논문에서는 신호원의 최대값을 추정해 이러한 한계를 극복하여 신호원의 분포를 복원할 수 있는 새로운 신호원 영상법을 제안하였다.

제안된 방법들을 다양한 상황의 시뮬레이션을 통해 정확도를 평가했으

며 간질환자의 데이터에 적용해 수술로 제거된 뇌부위와 뇌자도를 이용해 복원된 신호원의 위치와 분포영역을 비교하였다. 그 결과, 본 논문에서 제안한 방법들은 기존 방법에 비해 뇌자도 및 뇌전도의 국지화 정확도를 향상시켰 수 있었으며 앞으로 뇌영역 활성부위를 추정하는 의학 분야 및 역문제 연구에서 널리 사용될 것으로 기대된다.

주요어 : 생제전자기학, 신호원 복원법, 역문제, 비침습적 뇌기능영상법, 뇌전도, 뇌자도

학번 : 2008-30136